iScience

Article

Atypical plume-like events contribute to glutamate accumulation in metabolic stress conditions

Graphical abstract

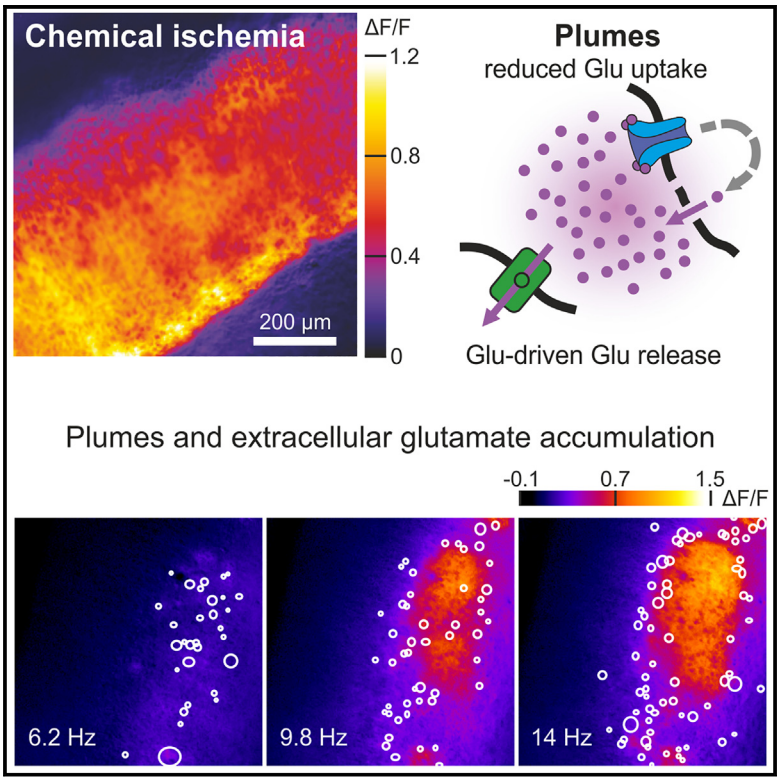

Highlights

- SF-iGluSnFR imaging shows plume-like glutamate release in cultured brain slices
- Plumes are TTX-insensitive and occur independently of neuronal network activity
- Plumes are favored by impaired glutamate uptake and suppressed by iGluR inhibition
- Plumes persist and contribute to glutamate accumulation during chemical ischemia

Authors

Tim Ziebarth, Nils Pape, Joel S.E. Nelson, ..., Hil G.E. Meijer, Christine R. Rose, Andreas Reiner

Correspondence

andreas.reiner@rub.de

In brief

Small molecule; Molecular network; Molecular neuroscience; Specialized functions of cells

Ziebarth et al., 2025, iScience *28*, 112256
April 18, 2025
https://doi.org/10.1016/j.isci.2025.112256

CellPress

iScience

CellPress
OPEN ACCESS

Article

Atypical plume-like events contribute to glutamate accumulation in metabolic stress conditions

Tim Ziebarth,[1,4] Nils Pape,[2] Joel S.E. Nelson,[2] Fleur I.M. van Alphen,[3] Manu Kalia,[3,5] Hil G.E. Meijer,[3] Christine R. Rose,[2] and Andreas Reiner[1,6,*]

[1]Department of Biology and Biotechnology, Ruhr University Bochum, Universitätsstrasse 150, 44801 Bochum, Germany
[2]Institute of Neurobiology, Heinrich Heine University Düsseldorf, Universitätsstrasse 1, 40225 Düsseldorf, Germany
[3]Department of Applied Mathematics, University of Twente, Drienerlolaan 5, 7522 NB Enschede, the Netherlands
[4]Present address: Hotchkiss Brain Institute, Department of Physiology and Pharmacology, Cumming School of Medicine, University of Calgary, Calgary, AB T2N 4N1, Canada
[5]Present address: Department of Mathematics and Computer Science, Free University of Berlin, Arnimallee 6, 14195 Berlin, Germany
[6]Lead contact
*Correspondence: andreas.reiner@rub.de
https://doi.org/10.1016/j.isci.2025.112256

SUMMARY

Neural glutamate homeostasis is important for health and disease. Ischemic conditions, like stroke, cause imbalances in glutamate release and uptake due to energy depletion and depolarization. We here used the glutamate sensor SF-iGluSnFR(A184V) to probe how chemical ischemia affects the extracellular glutamate dynamics in slice cultures from mouse cortex. SF-iGluSnFR imaging showed spontaneous glutamate release indicating synchronous network activity, similar to calcium imaging with GCaMP6f. Glutamate imaging further revealed local, atypically large, and long-lasting plume-like release events. Plumes occurred with low frequency, independent of network activity, and persisted in tetrodotoxin (TTX). Blocking glutamate uptake with TFB-TBOA favored plumes, whereas blocking ionotropic glutamate receptors (iGluRs) suppressed plumes. During chemical ischemia plumes became more pronounced, overly abundant and contributed to large-scale glutamate accumulation. Similar plumes were previously observed in cortical spreading depression and migraine models, and they may thus be a more general consequence of glutamate uptake dysfunctions in neurological and neurodegenerative diseases.

INTRODUCTION

Glutamate is key for transmitting signals across excitatory synapses. In the healthy brain, the extracellular glutamate concentrations are strictly regulated to provide the right dosage for activating synaptic glutamate receptors in a spatially and temporally defined manner.[1–3] However, the underlying processes, namely the vesicular release of glutamate from neurons, the astrocytic uptake of glutamate through excitatory amino acid transporters (EAATs),[4,5] the restoration of ion gradients, and glutamate metabolism[6] require substantial amounts of energy.[7]

Many pathological conditions are thought to involve dysregulation or disruption of neurotransmitter homeostasis that results in increased levels of extracellular glutamate and synaptic spillover.[1] Increased glutamate concentrations can interfere with normal synaptic transmission and plasticity. Higher doses of glutamate may cause overexcitation, disrupt cellular Ca^{2+} homeostasis, and trigger cell death mechanisms, which is commonly referred to as "excitotoxicity".[8–10]

An extreme situation is encountered under ischemic conditions, such as stroke. There, lack of blood and oxygen supply causes strong energy depletion, yet some aberrant neural activity persists in the penumbra, i.e., the tissue surrounding the infarct core.[11–13] This results in prolonged and repetitive depolarizations, deterioration of ion gradients, uncontrolled neurotransmitter release, impaired neurotransmitter uptake, acidification, swelling, and delayed cell death. These processes are thought to involve glutamate-mediated overactivation of ionotropic glutamate receptors (iGluRs). Indeed, suppression of AMPA and NMDA receptor activity, has been shown to be neuroprotective in experimental stroke models[8] and NMDA receptor activation is deemed particularly important for cell death and survival.[14,15] However, the extent to which glutamate contributes to the acute phase of metabolic stress, e.g., by promoting spreading depolarizations (SDs), remains controversial.[16]

Until recently, glutamate levels could only be deduced by rather indirect means, i.e., microdialysis or measurement of receptor currents.[17] The development of genetically encoded fluorescence-based sensors has enabled us to obtain more direct, spatially and temporally defined information on glutamate release and accumulation. Especially iGluSnFR (intensity-based glutamate-sensing fluorescent reporter)[18,19] variants are now

widely used to investigate stimulus-evoked release and spread of glutamate in different physiological paradigms[20–27] and in disease models,[28] including models of cortical SD,[29–31] epilepsy,[32,33] depression,[34] Alzheimer's,[35–37] and Huntington's disease.[38–40]

Here, we set out to study the extracellular glutamate dynamics during metabolic stress conditions using a defined *in situ* model, in which we induced brief chemical ischemia in organotypic slice cultures from mouse cortex. Previous work had shown that this model recapitulates key features of the ischemic penumbra, such as reversible ATP depletion from cells and an increase in intracellular Na^+ and extracellular K^+ concentrations.[41–44] In this study, we measured neuronal activity and changes in the extracellular glutamate concentration to study how glutamate release and uptake are altered in energy-scarce conditions.

Imaging of SF-iGluSnFR(A184V) expressed on the surface of neurons showed different types of glutamate dynamics, namely global synchronous network activity and atypical local glutamate events. The latter are reminiscent of recently described "plume-like" events.[31] Brief chemical ischemia resulted in a transient loss of synchronous network activity, yet a strong increase in the occurrence of plumes and pronounced extracellular glutamate accumulation. Plumes were favored by blocking glutamate uptake and they were suppressed by inhibiting iGluRs, which points to a feedforward mechanism, in which elevated levels of glutamate trigger plume-like glutamate release events. The emergence of plumes deserves further investigation, as they might also occur under less severe pathological conditions.

RESULTS

Chemical ischemia in an organotypic slice model

To investigate the effects of metabolic stress on the extracellular glutamate dynamics, we prepared cortico-hippocampal slice cultures from mice and expressed the genetically encoded fluorescent glutamate sensor SF-iGluSnFR(A184V)[19] under control of a synapsin promoter (hSyn1) using recombinant adeno-associated virus particles (rAAVs). After 14–21 days expression *in vitro*, sensor fluorescence was seen throughout all cortical layers (Figure 1A). Healthy slices showed spontaneous, synchronized activity, as seen by spikes in fluorescence intensity (0.19 ± 0.11 Hz, mean ± SD, n = 11 slices; Figures 1B–1H) that occurred globally across the whole imaged region. This epileptiform network activity is characteristic for slices of this age[45,46] and was also observed by neuronal Ca^{2+} imaging using GCaMP6f (Figures 1I–1M, 0.16 ± 0.10 Hz, mean ± SD, n = 8 slices).

To mimic energy restriction as it might occur in the ischemic penumbra, we induced transient chemical ischemia by removing glucose and adding 2 mM 2-deoxy-D-glucose and 5 mM sodium azide to block glycolysis and mitochondrial electron transport, respectively (Figure 1B).[47] After 2–5 min, we switched back to normal Ringer's solution. Inducing chemical ischemia for 2 min caused a transient decrease of the intracellular ATP concentration, as seen by a 18.8 ± 2.6% fluorescence ratio decrease of the FRET-based ATP sensor, ATeam1.03^{YEMK} ("ATeam")[44,48,49] compared to baseline levels (mean ± SD, n = 39 cells in 4 slices; Figure S1). Inducing chemical ischemia for 5 min strengthened the drop in the ATeam fluorescence ratio to 54.1 ± 8.0% (n = 23 cells in 3 slices). The neuronal ATP levels recovered as the ATeam ratio returned to the initial baseline within ~10 min after washout (Figure S1).

Energy restriction had pronounced effects on the SF-iGluSnFR signals. Within 2 min after inducing chemical ischemia, the global fluorescence signals reporting synchronous activity had fully ceased in all regions. Still, somewhat later, a sustained increase in SF-iGluSnFR fluorescence was seen, which started locally and eventually spread across extended areas of the slice (Figures 1B–1D and Video S1). We attribute this signal increase to an overall increase in extracellular glutamate concentration, since SF-iGluSnFR does not respond to any other neurotransmitters.[18] In addition, control experiments confirmed that (1) SF-iGluSnFR is minimally affected by the applied azide and that (2) acidification of the extracellular space, which often accompanies ischemia,[50] would decrease rather than increase the baseline fluorescence and signal amplitude (Figure S2A).

The half-maximal signal rise in glutamate accumulation (50% rise) was observed 4.03 ± 0.92 min after inducing ischemia (mean ± SD, n = 11 slices). The fluorescence increase started and was most pronounced in more central regions of the slices. At the peak of the accumulation, the relative fluorescence increase of the responding area was $\Delta F/F$ = 0.31 ± 0.19 (mean ± SD, n = 11 slices; Figure 1G). In some cases, the fluorescence intensity during accumulation exceeded the signal changes associated with synchronous activity. In some areas the intensity was even as high as during a control application of a highly saturating glutamate concentration (10 mM) (Figure S4). However, regions that responded most strongly to bath-applied glutamate, showed no or little glutamate accumulation during ischemia (Figures S4B and S4C). This indicates that the observed glutamate accumulations might depend on the degree of bath coupling (see Figures S5–S7 and STAR Methods), i.e., deeper or more dense regions of the slice, which have less bath exchange, may show more glutamate accumulation during ischemia.

Upon reperfusion with normal Ringer's solution the glutamate accumulation decayed within 4.21 ± 2.67 min (time to half-maximal signal decay; mean ± SD, n = 11 slices). Global synchronous events reappeared 7.28 ± 1.45 min after washout (mean ± SD, n = 11 slices). The decreased signal amplitudes at these late time points (Figure S8D) might be in part attributable to changes in the SF-iGluSnFR fluorescence properties, since a run-up of the baseline intensity and decreased event amplitudes were also seen in 40 min control recordings without inducing chemical ischemia (Figure S9) and also HEK cell experiments (Figure S3).

Besides extracellular glutamate accumulation, chemical ischemia resulted in a strong increase in neuronal GCaMP6f fluorescence, which indicates extensive Ca^{2+} loading (see also Video S2). The onset of neuronal Ca^{2+} loading (3.38 ± 1.17 min to half-maximal signal rise, mean ± SD, n = 8 slices) and duration (Figures 1K and 1L) were comparable to extracellular glutamate accumulation (Figures 1E and 1F). After reperfusion with standard Ringer's solution synchronous activity returned (first events 4.94 ± 0.92 min after washout, mean ± SD, n = 8 slices) albeit with slower decay times (Figure S8E).

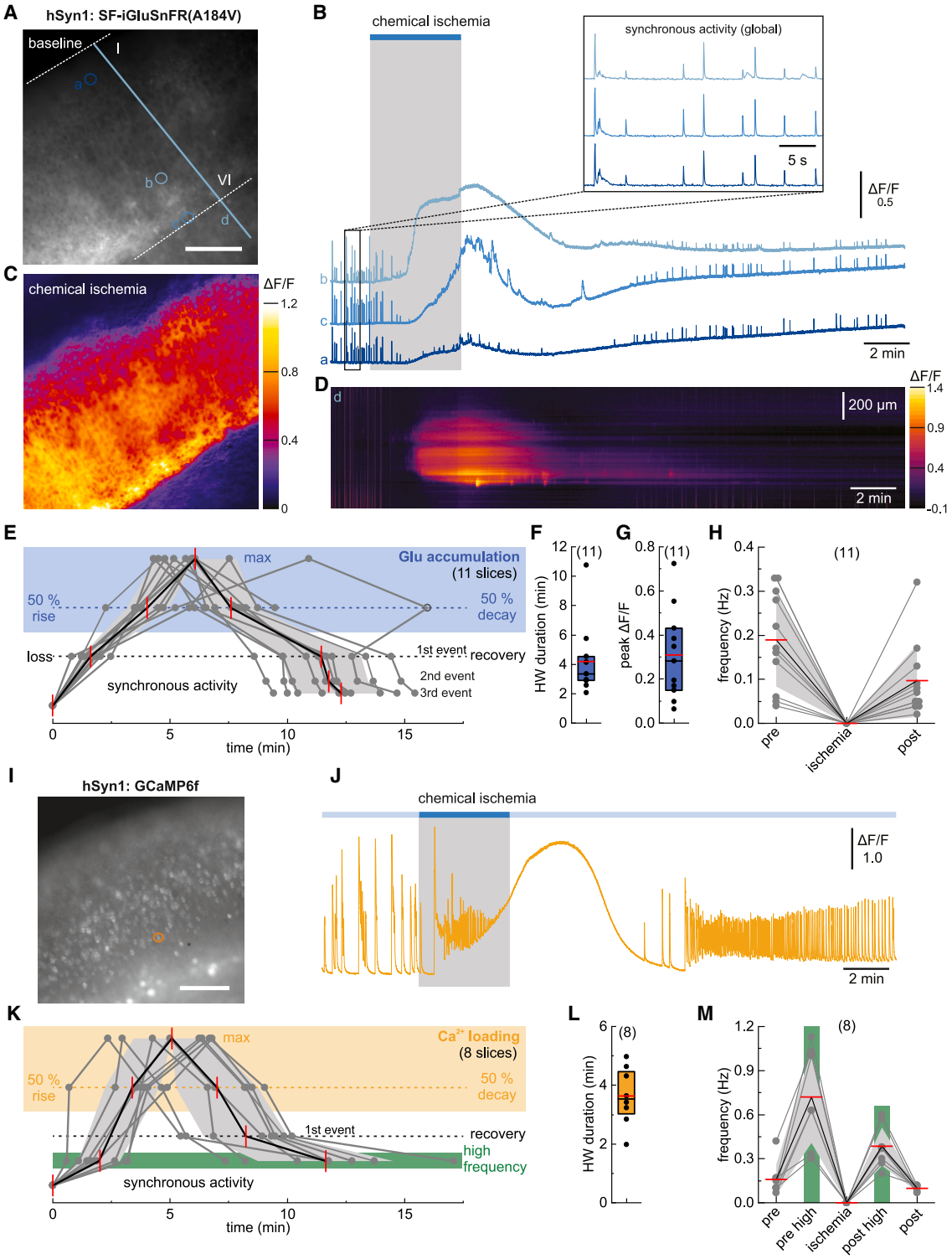

Figure 1. Optical probing of chemical ischemia in organotypic slice cultures from mouse cortex

(A) SF-iGluSnFR(A184V) widefield imaging of cortical layers. Scale bar: 200 µm.

(B) Relative fluorescence changes (ΔF/F) of selected regions (a–c in A) show a reversible loss of global synchronous activity and large-scale glutamate accumulation upon inducing chemical ischemia (no glucose, 2 mM 2-deoxy-D-glucose and 5 mM sodium azide for 2–5 min).

(C) Glutamate accumulation during chemical ischemia (ΔF/F image, region as in A).

(D) Temporal ΔF/F profile along the line region d in (A).

(legend continued on next page)

A notable difference between the Ca^{2+} and Glu dynamics was seen in the early phase of ischemia. Here, Ca^{2+} imaging showed a high-frequency period, i.e., increased spontaneous activity, 1.96 ± 0.88 min after inducing ischemia (mean ± SD, n = 8 slices), which coincided with the beginning of intracellular Ca^{2+} loading (Figures 1J and 1K). In contrast, spontaneous glutamate release events decreased in signal amplitude and became fully undetectable already 2.57 ± 1.10 min before large scale glutamate accumulation set in (mean ± SD, n = 11 slices, Figures S8A–S8C). This suggests that in the early ischemic period the amount of glutamate released during synchronous activity decreased and eventually became undetectable, whereas intracellular Ca^{2+} showed continuing oscillatory activity. During recovery a second high-frequency Ca^{2+} period was seen (8.51 ± 2.26 min after washout, mean ± SD, n = 8 slices), i.e., around the time when the first synchronous glutamate events reappeared (Figures 1B–1E). Autonomous, high-frequency neuronal activity is typically seen at intermediate depolarization levels, as also seen in our simulations (STAR Methods; Figure S6, and Kalia et al. [51]).

Taken together, these results show that the applied chemical ischemia protocol causes transient ATP depletion and Ca^{2+} accumulation in neurons, transient disruption of synchronous network activity, and yet strong glutamate accumulation in the extracellular space.

SF-iGluSnFR imaging shows local glutamate events under baseline conditions

Under baseline conditions, SF-iGluSnFR widefield imaging showed global, synchronous network activity, as described previously. The signal changes were rather uniform across all cortical layers (Figure 2, average intensity projection) and the events had fast and rather uniform characteristics. Their kinetics were not fully resolved by our 20 fps standard imaging rate and bursting behavior became more apparent at 99 fps (Figure S11). As described above, these synchronous glutamate release events showed similar frequencies as Ca^{2+} events (Figure 1H,M) and appear to reflect spontaneous network activity, which is typical for organotypic slices at this age.[45,46]

Unexpectedly, the imaging data revealed also another type of activity—local, asynchronous glutamate release events, which were seen in baseline conditions and far more prominently during ischemia and recovery. In the following, we characterize these events in more detail.

Under baseline conditions (pre-ischemia), local glutamate release events were clearly discernible from global synchronous activity (Figures 2 and S10, and Video S3). They were asynchronous, limited to small regions, and quite heterogeneous in size and duration (Figure 2A). In order to collect these events, we calculated maximum intensity projections over 25–100 s (excluding frames which contained synchronous activity) and analyzed all identifiable events in the imaged region (see STAR Methods for details). In the field-of-view (824 × 824 μm^2 = 0.679 mm^2), we captured local events with a median frequency of 1.04 Hz (n = 11 slices; Figures 2E and S12), but the frequency varied strongly between slices (0.06–4.92 Hz). Smaller, less intense, or shorter events might have escaped our detection. In seven other slices, we detected no plumes under pre-ischemic baseline conditions.

The captured local events had a half-width duration of 267 ± 190 ms (mean ± SD; n = 296 events), i.e., most of these events lasted considerably longer than synchronous events (Figure 2F). The average signal amplitude ΔF/F of local events was 0.07 ± 0.05 (mean ± SD; n = 296 events), which is much lower than typical ΔF/F values of synchronous activity in the same region (Figures 2G and 2H). Still, for some local events the signal increase exceeded the signal change during synchronous activity. Based on their long-lasting but transient properties we refer to these local events as glutamate "plumes", a term that was recently introduced by Parker et al.[31]

Analysis of individual movies showed that plumes occurred independently of synchronous activity (Figures 2D and S10C), which was also confirmed by analyzing the time delays between synchronous events and plumes (Figure S10D), and their frequencies in different slices (Figure S10E).

Local glutamate events ("plumes") have unique properties

We next characterized the spatial and temporal characteristics of individual plumes that we had observed under baseline conditions (pre-ischemia). To determine plume sizes, we used the frame with the maximal plume ΔF/F to measure the full-width at half-maximum (FWHM) in x and y direction, which revealed an aspect ratio of ~1 (1.02 ± 0.20; mean ± SD, n = 296), i.e., plumes had an overall roundish appearance (Figures 3A and 3B). Elongated shapes were mostly obtained for small plumes, which might be due to their less precise detection. The mean FWHM size was 17.2 ± 6.4 μm (mean ± SD, n = 296). Very large plumes had FWHM sizes of 38.6 μm or more. The lowest plume size was 6.44 μm, which reflects our detection limit (see STAR Methods).

The rise times of individual plumes were rather fast (129 ± 160 ms; 10–90% signal change, mean ± SD, n = 296; Figure 3C) and close to the temporal detection limit of our recordings. The plume decay times were considerably slower (440 ± 361 ms;

(E) Time points of loss and recovery of synchronous activity and glutamate accumulation (50% rise, maximum, and 50% decay times) for n = 11 slices.
(F) Half-width duration of glutamate accumulation.
(G) Peak ΔF/F of responding regions.
(H) Frequency of synchronous Glu events before, during, and after ischemia (50% decay time +10 min).
(I) GCaMP6f imaging. Scale bar: 200 μm.
(J) ΔF/F trace showing increased synchronous activity before and after chemical ischemia, and neuronal Ca^{2+} loading during ischemia.
(K) Time points of high frequency periods, Ca^{2+} loading, and recovery of synchronous activity for n = 8 slices.
(L) Half-width duration of Ca^{2+} loading.
(M) Frequency of synchronous Ca^{2+} activity.
In all data panels, individual data points are shown in gray, mean values in red and SD as shaded areas. Boxes show medians and 25–75% percentiles. For details see STAR Methods.

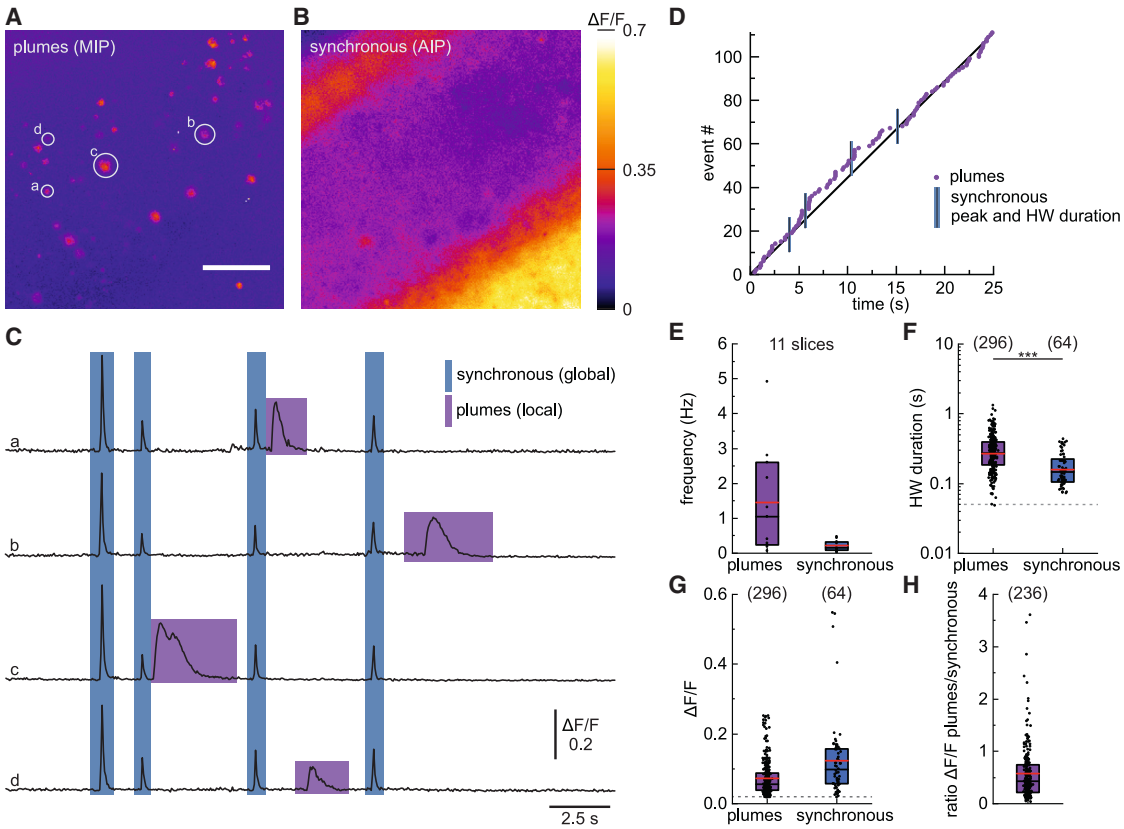

Figure 2. SF-iGluSnFR(A184V) imaging shows local glutamate events ("plumes") which occur independently of synchronous network activity

(A) Local glutamate plumes as seen in a maximal intensity projection (MIP; 25 s, excluding frames with synchronous activity). Scale bar: 200 μm.

(B) Global fluorescence changes during synchronous activity (average intensity projection (AIP) of frames containing the event maxima; region as in A).

(C) ΔF/F traces of four selected regions (a-d). Plumes are local, but synchronous events are seen in all regions (cf. B).

(D) Time points of plume occurrence and synchronous activity. Data (A)–(D) were taken from the pre-ischemic baseline of the slice shown in Figures 1A–1D.

(E) Frequencies of plumes and synchronous activity from $n = 11$ slices under baseline conditions.

(F) Half-width durations of plumes and synchronous activity from $n = 11$ slices. A Mann-Whitney U test was used for pairwise comparison, $^{***}p < 0.001$.

(G) Maximum ΔF/F values from $n = 10$ slices.

(H) Most plumes show smaller ΔF/F values than synchronous activity in the same region.

(F–H), numbers in parentheses give the number of analyzed events, dashed lines show the detection limits. Boxes show medians and 25–75% percentiles, red bars indicate the mean.

mean ± SD, $n = 296$). A comparison of different plume parameters reveals a moderate correlation between plume size and duration (Spearman coefficient $r = 0.56$, 296 plumes, Figure S13), but weaker correlations between plume size and plume intensity ($r = 0.40$), and between plume intensity and duration ($r = 0.36$), indeed, some short plumes showed high signal changes.

Example plumes with different characteristics are shown in Figures 3D–3G. Cross-sections show that the highest ΔF/F amplitudes were found in the plume center. However, in large plumes the area with maximal signal changes extended over 10 μm or more (cf. Figure 3F), which could either reflect a homogenous glutamate distribution or SF-iGluSnFR saturation.

The plume properties were rather uniform across different slices (Figure S12) and their key characteristics did not significantly change during 40 min continuous control recordings without inducing ischemia (Figure S14). Only the plume intensity ΔF/F decreased to 75%, which is similar to the signal loss seen for synchronous events (cf. Figure S8), while the plume frequency decreased to 56% ($n = 5$ slices, Figure S14).

To test whether plumes depend on action potential-driven release we added the sodium channel blocker tetrodotoxin (TTX). Perfusion of 0.2 μM TTX for 4 min resulted in a complete loss of global synchronous activity, but plumes were left largely unaffected (Figures 4A-4C and S15). Plumes were observed throughout the recording and their size, duration, and intensity (ΔF/F) remained unchanged (Figure S15). The decrease in plume frequency was comparable to control. After TTX washout, synchronous glutamate release events (and Ca^{2+} events) returned with increased signal amplitudes ΔF/F (Figure S15), most likely due to upscaling.[52] Plume size was slightly increased, but the other plume characteristics remained unchanged.

We next aimed to strengthen network activity by inhibiting $GABA_A$ receptors with 3 μM (GBZ).[53] Indeed, GBZ addition increased the signal amplitudes of global synchronous glutamate

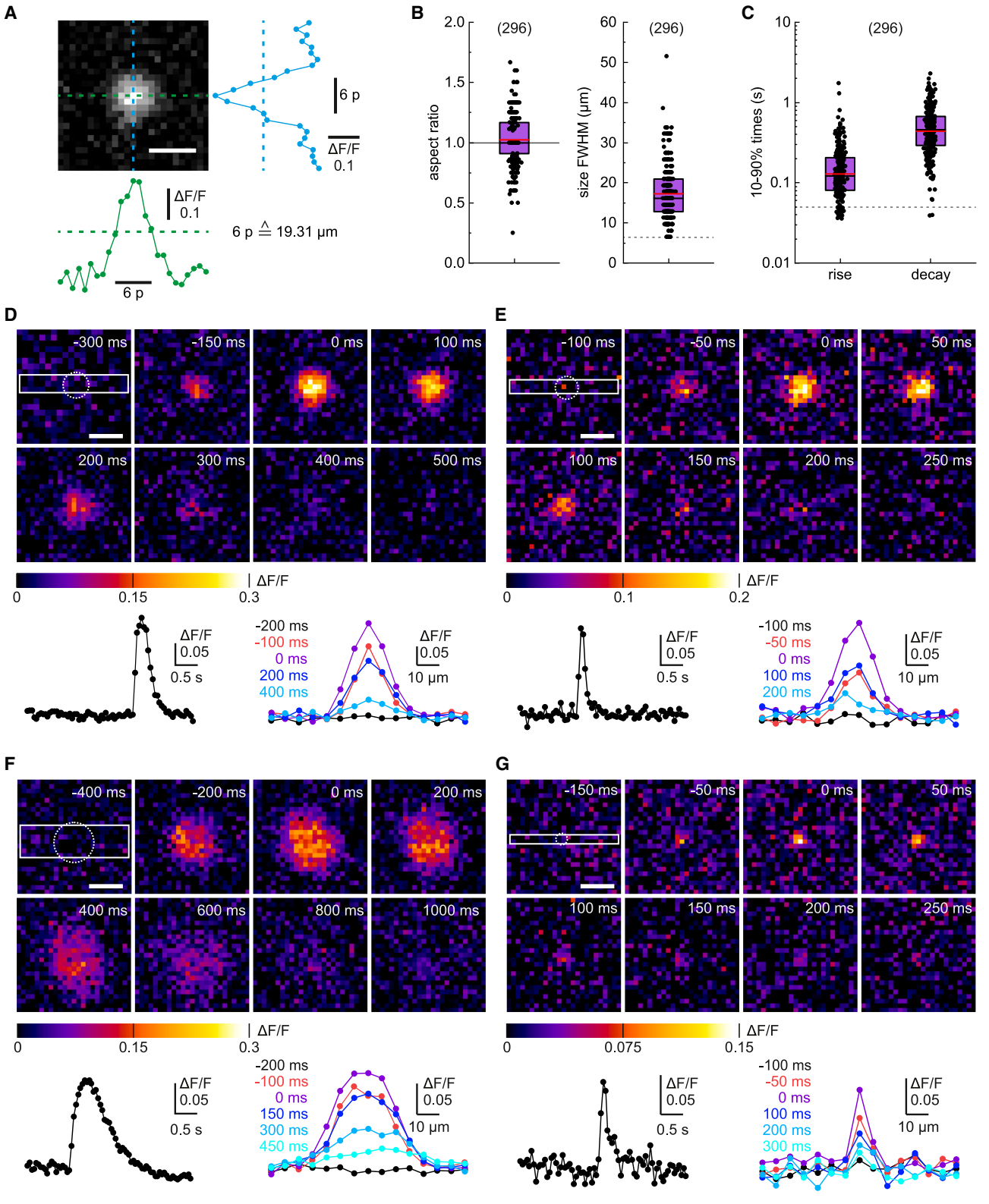

(legend on next page)

release events and Ca^{2+} signals (Figure S16), probably by reducing inhibitory inputs.[54] However, also this manipulation did not change plume frequency or individual plume parameters compared to baseline (Figures 4E and S16).

Next, we tested the role of glutamate uptake by adding TFB-TBOA, which blocks the glutamate transporters EAAT1, EAAT2, and to some extent also EAAT3.[55] Impaired glutamate uptake should prolong the synchronous glutamate transients and might affect network activity,[18,20,24,56,57] but it might also affect plumes directly. As expected, addition of 1 μM TFB-TBOA (Figures 5A–5D) had pronounced effects on synchronous activity resulting in prolonged glutamate events, more bursting behavior, and larger event amplitudes (n = 7 slices). The frequency of synchronous events temporarily decreased in most slices (Figure S17B). The same effects were seen when monitoring Ca^{2+} influx (n = 5 slices; Figure S17C). Notably, TFB-TBOA had a strong effect on the occurrence (induction) of plumes: TFB-TBOA resulted in a 6- to 73-fold increase in plume frequency at times at which synchronous event frequencies were decreased and it induced plumes in three slices that had not shown plumes before (Figures 5A, 5B, and S17, and Video S6). Plume intensity (ΔF/F) or decay times (Figure 5C) were not affected by TFB-TBOA, but a minor increase in rise time and a clear increase in plume size (1.3-fold increase in FWHM; Figure S17) was observed.

The strong frequency increase in plume occurrence seen with TFB-TBOA suggested that elevated extracellular glutamate concentrations themselves might contribute to the induction of plumes. This prompted us to test whether plume induction was dependent on iGluR activation. Indeed, inhibiting AMPA and NMDA receptors by coapplying 50 μM GYKI 53655 and 25 μM D-AP5, respectively[58,59] caused a strong reduction in plume frequency within 4 min (to 25 ± 13%, mean ± SD, n = 4 slices) that returned to control levels after washout (Figures 5E–5G and S18). The addition of only D-AP5 to just block NMDA receptors resulted in a lower decrease to 37 ± 7% (after 4 min, n = 4 slices) (Figure 5I).

"Plume-like" glutamate events contribute to glutamate accumulation during chemical ischemia

Having observed and characterized plumes in pre-ischemic baseline conditions, we next asked how these events change upon inducing chemical ischemia and how they contribute to the observed large-scale accumulation of glutamate (cf. Figures 1B–1G). For this, we analyzed different episodes leading up to glutamate accumulation and during recovery, as shown for a typical example in Figures 6A–6C, S21, and S22.

As described previously, the onset of the ischemic period was characterized by a loss of global synchronous activity some time before extracellular glutamate accumulation occurred (Figure 6B). After synchronous activity had ceased, more and more plumes were detected (Figure 6C). Over time, regions with a high incidence of plumes showed a gradual fluorescence increase. When the global glutamate accumulation had reached 50% of the maximal accumulation (ΔF/F), the plume frequency had increased 7.0-fold compared to baseline (5 s or 25 s time windows, n = 11 slices, Figure 6D). Eventually, the central regions reached a maximum fluorescence signal, which also meant that individual events became indiscernible, possibly due to sensor saturation in these regions (Figure 6C). However, plume-like dynamics were still seen at the edges of these regions and plumes were abundantly detected in less saturated regions (see Videos S1 and S7). High plume activity was also uncovered when the fluorescence intensity gradually decreased during recovery (decay). The plume frequencies only decreased later, about 4 min after the accumulation had decayed to the 50% mark. Around that time also global synchronous release events reappeared (Figure 1E). Eventually, the plume frequency returned to baseline levels (Figure 6D). Control measurements without inducing ischemia showed a steady decrease in plume frequency over 40 min (Figure S14).

Chemical ischemia also had pronounced effects on plume size and duration. The plume size increased 1.4-fold, from 18 ± 7 μm before ischemia to 25 ± 10 μm during ischemia (at 50% rise, mean ± SD) (Figure 6E). Plume half-width duration increased from 317 ± 331 ms before ischemia to 576 ± 592 ms (mean ± SD) (Figure 6F). The longer duration was attributable to both, longer rise and longer plume decay times (Figure S22). Despite the post-ischemic normalization of plume frequency, the plume size and also plume duration remained elevated at later time points, suggesting that persistent changes in glutamate homeostasis might have occurred.

These data suggest that local, plume-like events contributed to glutamate accumulation during chemical ischemia. Plumes are apparently favored by ischemic conditions, as a high number of plumes became observable along with significant changes in their properties. Notably, plumes persisted during periods of maximal energy depletion, while synchronous network activity did not.

A notable observation is also provided by slices, which showed regions with elevated glutamate concentrations after cultivation (Figures 6G and S21). In the vicinity of these "defect" regions, atypically large plumes were already observed at a high rate before inducing chemical ischemia (Figure 6G). Later, during chemical ischemia, these defect regions acted as nuclei for sustained glutamate accumulation (Figure 6H).

Since we had found that plumes can be suppressed by inhibiting iGluRs (Figures 5E–5I), we used this to test their contribution to extracellular glutamate accumulation during chemical

Figure 3. Spatial and temporal characteristics of local plumes

(A) Example plume with ΔF/F cross-sections. Scale bar: 25 μm.

(B) Aspect ratio and mean full-width at half maximum (FWHM) obtained from ΔF/F images at the peak maximum for n = 296 plumes from 11 slices pre-ischemia (see also Figure S12). Boxes show medians and 25–75% percentiles, red bars indicate the mean.

(C) Rise and decay times (10–90%) obtained from ΔF/F traces of individual plumes. Boxes show medians and 25–75% percentiles, red bars indicate the mean.

(D–G) Depiction of four individual plumes with different spatial and temporal characteristics. ΔF/F time traces (left) obtained from the circled regions. Spatial profiles at different time points (right) are based on the boxed regions. Time zero reflects the plume maximum. For image processing see Figure S13. Scale bars: 25 μm.

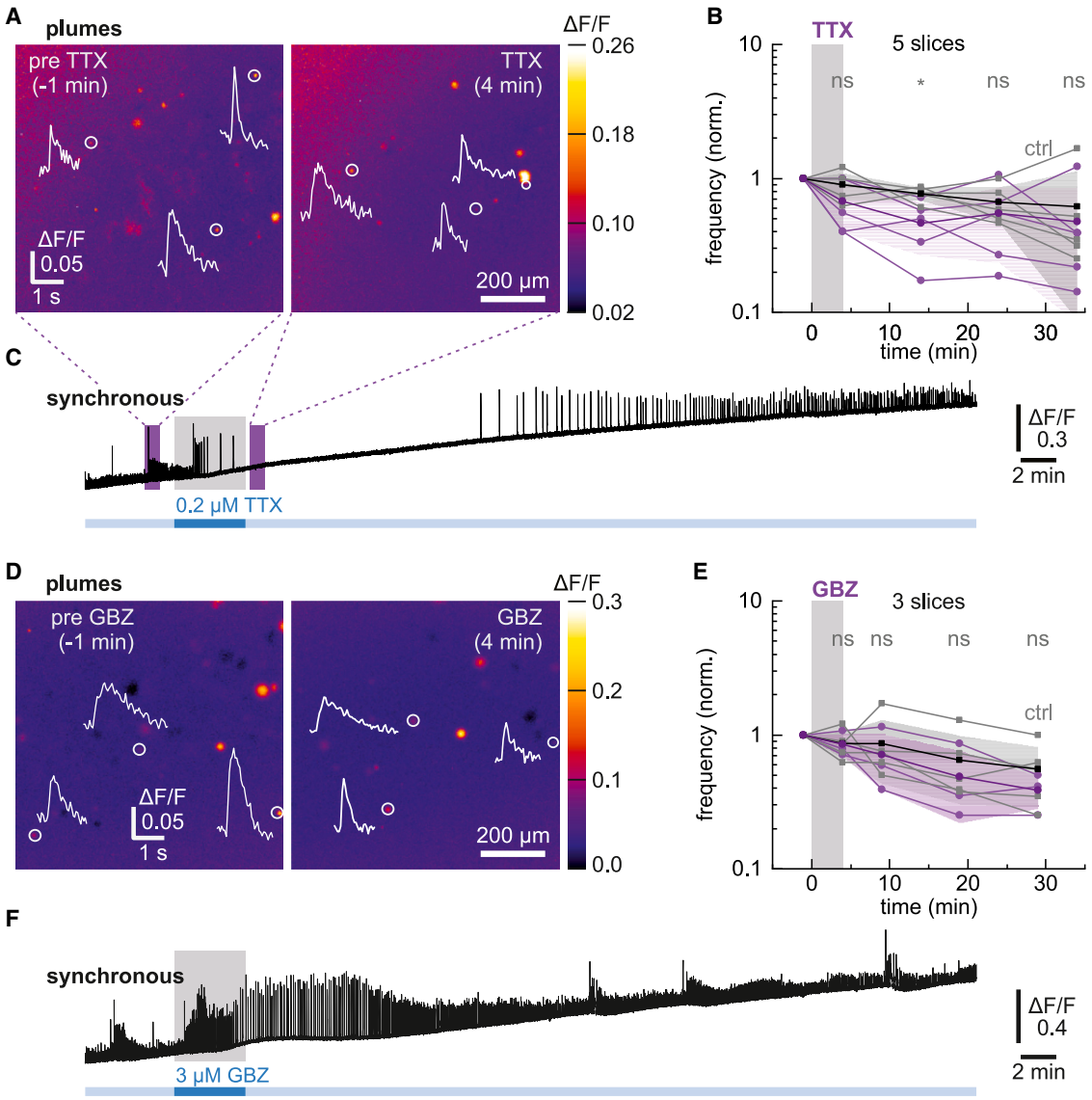

Figure 4. Plumes after blocking network activity with TTX or strengthening network activity with GBZ

(A) Plumes remained detectable after addition of 0.2 µM TTX (maximal intensity projections, 50 s each with traces of selected plumes). Scale bar: 200 µm.

(B) Plume frequency at selected time points (n = 5 slices, purple) in comparison to control recordings without TTX (n = 5 slices, black). Data points are shown in light color, means in dark with SD as shaded areas. Mann-Whitney U tests were used for pairwise comparison of individual time windows to control (cf. Figure S14), ns not significant, *$p < 0.05$.

(C) Synchronous activity was suppressed by TTX. For details see Figure S15.

(D) Plumes before and after addition of 3 µM GBZ. Scale bar: 200 µm.

(E) GBZ did not change the plume frequency (n = 3 slices, purple) compared to control (n = 5 slices, black). Statistics and data representation as in (B). For other parameters see Figure S16.

(F) GBZ strengthened synchronous activity.

ischemia. Indeed, pre-application of both 50 µM GYKI 53655 and 25 µM AP5 for 4 min strongly suppressed the plume frequency increase and glutamate accumulation during 5 min chemical ischemia (Figures 7A–7E), whereas pre-application of 25 µM AP5 had a partial effect (Figures 7C–7E). Both, plumes and glutamate accumulation, were seen when we induced a second control chemical ischemia after removing the iGluR inhibitors. This suggested that iGluRs play a key role in driving plume formation and that plumes may contribute to the accumulation of glutamate in metabolic stress conditions.

DISCUSSION

In this study, we used chemical ischemia in organotypic slices to investigate how metabolic stress affects network activity and glutamate homeostasis. Previous work in this paradigm had

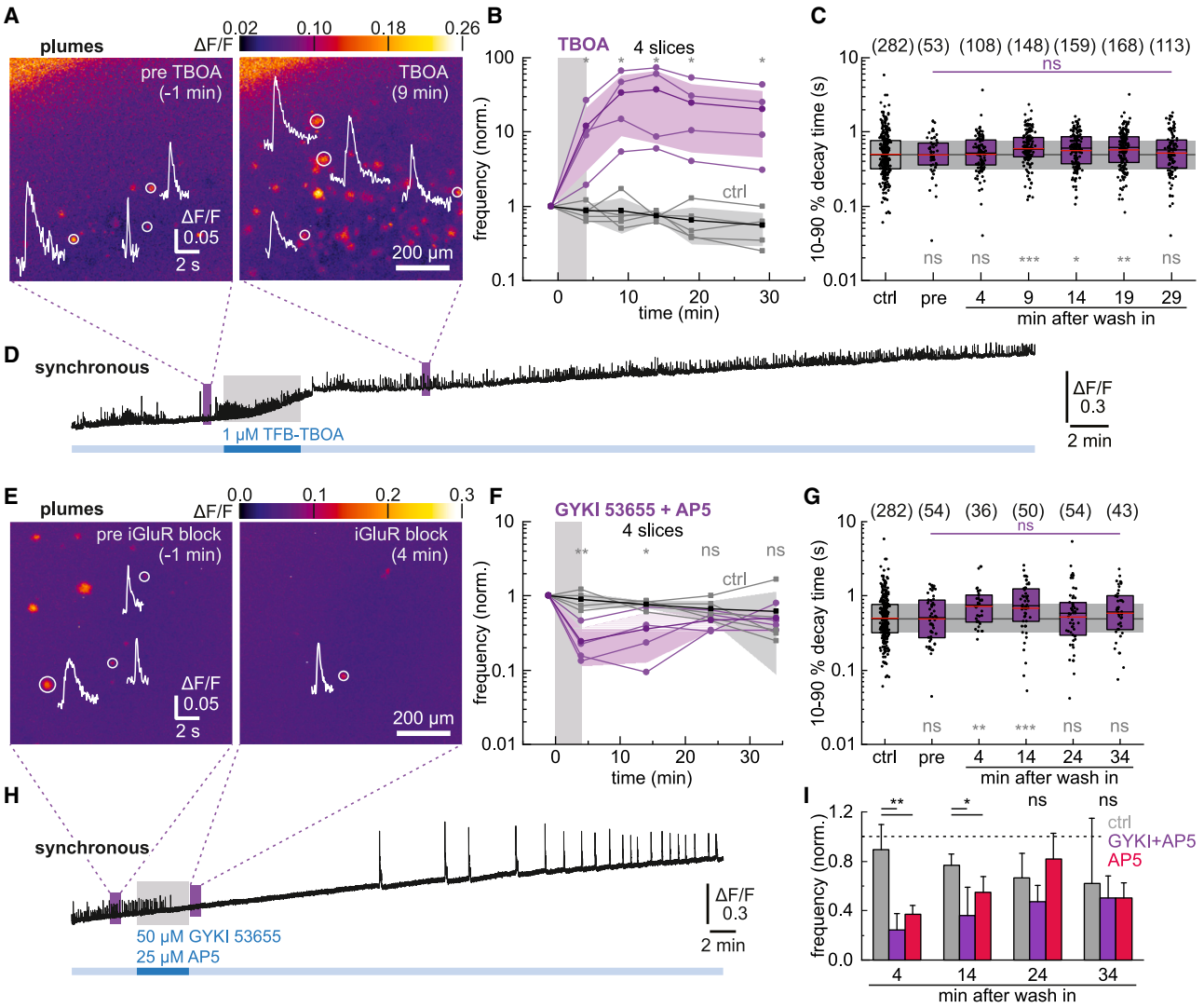

Figure 5. Plume characteristics after blocking glutamate uptake with TBOA or inhibition of iGluRs

(A) Addition of 1 µM TFB-TBOA increased the number of plumes (maximal intensity projections, 25 s each with traces of selected plumes). Scale bar: 200 µm.

(B) Plume frequency at selected time points ($n = 4$ slices, purple) in comparison to control recordings without TBOA ($n = 5$ slices, black). Individual measurements are shown in light color, means in dark, and SD as shaded areas. Mann-Whitney U tests were used to test for pairwise comparison of individual time windows to control, $^{*}p < 0.05$.

(C) Plume 10–90% decay times for the indicated time windows ($n = 7$ slices). Boxes show medians and 25–75% percentiles, red bars indicate the mean. Numbers in parentheses give the number of analyzed events. Mann-Whitney U tests were used for pairwise comparison of individual time windows to control (gray; cf. Figure S14), Kruskal-Wallis tests were used to test for differences between the six different time windows, followed by Dunn's test (purple), ns not significant, $^{*}p < 0.05$, $^{**}p < 0.01$, $^{***}p < 0.001$.

(D) Synchronous activity during the experiment. For quantifications see Figure S17.

(E) Addition of 50 µM GYKI 53655 and 25 µM D-AP5 reduced the number of plumes (maximal intensity projections, 50 s each with traces of selected plumes). Scale bar: 200 µm.

(F) Plume frequency at selected time points ($n = 4$ slices, purple) in comparison to control recordings without blockers ($n = 5$ slices, black). Statistics and data representation as in (B); ns not significant, $^{*}p < 0.05$, $^{**}p < 0.01$.

(G) Plume 10–90% decay times for the indicated time windows. Statistics and data representation as in (C).

(H) Synchronous activity was abolished by iGluR block. See also Figure S18.

(I) Addition of just 25 µM D-AP5 reduced the plume frequency partially (mean with SD, $n = 4$ slices, see Figures S19 and S20). Two-sample t tests were used for pairwise comparison of individual time windows to control, ns not significant, $^{*}p < 0.05$, $^{**}p < 0.01$.

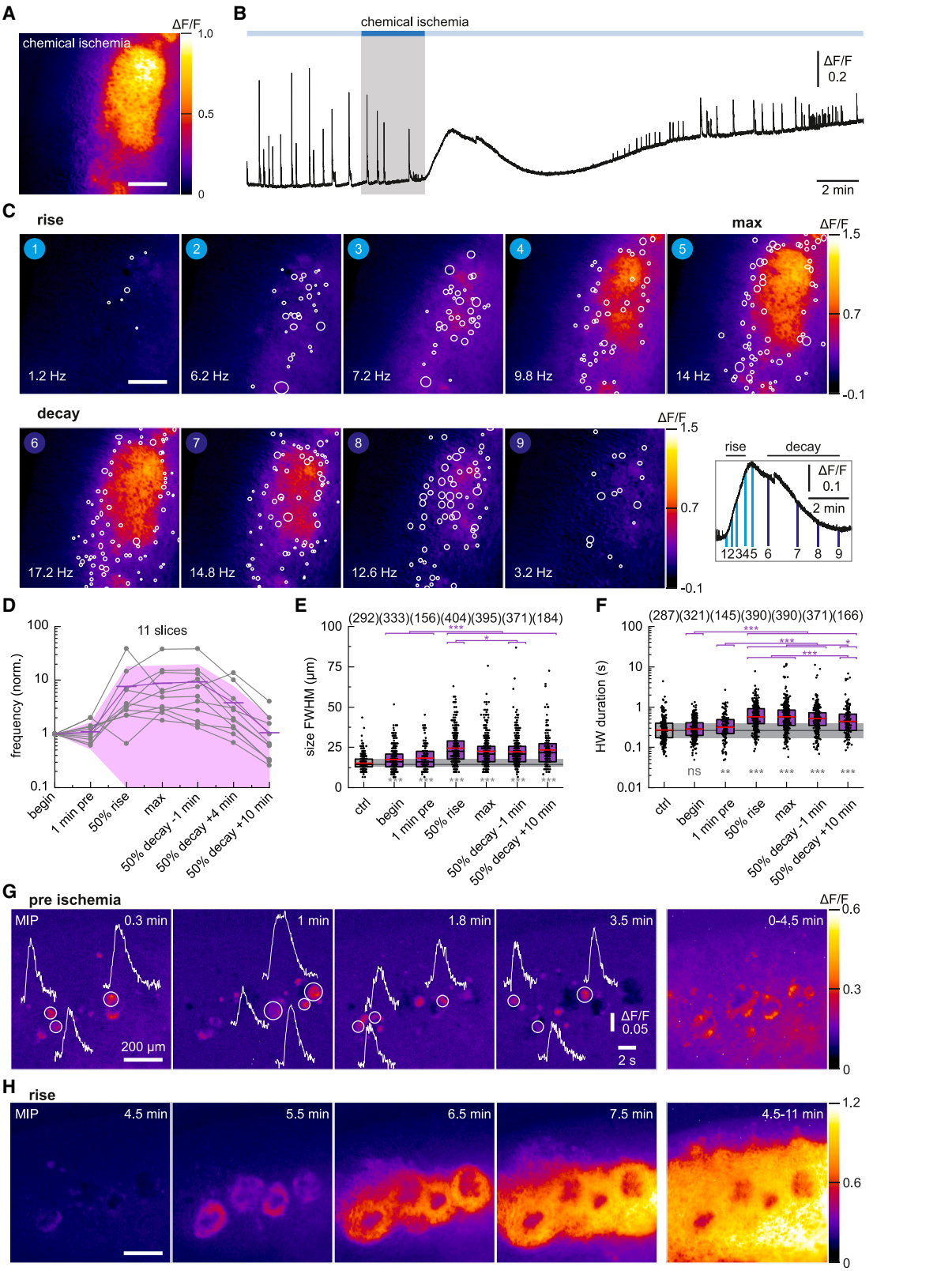

(legend on next page)

shown that brief energy depletion causes strong, yet reversible effects, namely astrocyte depolarization, increases of intracellular Na^+ and extracellular K^+ concentrations,[41–43] and intracellular ATP depletion.[44] Additional measurements with the fluorescent ATP sensor ATeam1.03^{YEMK} performed here (Figure S1), in combination with earlier *in situ* calibrations[49] and assuming a resting ATP concentration of 2.8 mM,[44] indicated that inducing chemical ischemia for 2 min resulted in a transient decrease in ATP concentration by ~1.2 mM. Inducing chemical ischemia for 5 min caused a ~2.6 mM decrease in ATP concentration, i.e., almost complete ATP depletion. Still, neurons almost fully regained their pre-ischemic ATP levels. Similarly, all other effects investigated here, i.e., the effect of chemical ischemia on neuronal network activity, neuronal Ca^{2+} loading, and extracellular glutamate dynamics, were mostly reversible (Figure 1). This suggests that our protocol mimics mild to moderate transient metabolic stress as it is encountered in the penumbra of an infarct core.[12,47,60]

Monitoring synchronous network activity with SF-iGluSnFR before and during chemical ischemia

Widefield SF-iGluSnFR(A184V) imaging reported on global synchronous network activity similar to GCaMP6f (Figures 1B,1H, 1J, 1M, S8, and S9). As expected, the measured glutamate transients decayed faster than the intracellular GCaMP6f signals. These events were not fully resolved at our imaging rates of 20 fps and 99 fps and some measured ΔF/F peak intensities may thus remain underestimated. The fast kinetics are in line with the high temporal resolution of SF-iGluSnFR(A184V) and were also reported for measurements of evoked release events.[19–21,24,25] Some events showed clear bursting behavior (Figure S11).

Our SF-iGluSnFR(A184V) measurements of synchronous activity were sensitive enough to detect an increased glutamate release upon recovery from TTX applications (Figures 4C and S15B). This increase could be either explained by rapid upscaling of synaptic glutamate release or network effects. Similarly, neuronal Ca^{2+} influx was strongly increased after TTX treatment (Figure S15C). Also, blocking $GABA_A$ receptors with gabazine increased the amount of released glutamate (Figures 4F and S16). This can be explained by either higher burst frequencies, prolonged bursts, and/or inclusion of more neurons into the network due to disinhibition.[61] In the early phase of gabazine addition, the latter two explanations appear to be more likely, since the highest signal amplitudes were observed while the event frequency was still low.

As expected, blocking glutamate uptake with TFB-TBOA had pronounced effects on synchronous events (Figure S17). Half-width duration, decay times and event amplitudes were strongly increased, all of which can be explained by reduced EAAT-mediated glutamate uptake.[18,20,24] In some slices, TFB-TBOA eventually reduced the frequency of synchronous events (Figure S17), which indicates that synaptic transmission became impaired. Blocking iGluRs with GYKI 53655 and D-AP5 resulted in a complete loss of network activity, which, after washout, continued with enhanced glutamate transients at low frequency (Figures 5H and S18). In summary, we find that SF-iGluSnFR (A184V) faithfully reports on synchronous network activity in slice cultures, which could be further utilized to study e.g., network maturation or regulation of epileptiform activity.

We next focused on how synchronous activity was affected by chemical ischemia. Synchronous SF-iGluSnFR signals were lost upon transient energy depletion (Figure 1), which was mostly due to a loss of signal amplitude. The signal amplitudes gradually decreased, while in some slices the event frequency increased in this period (Figure S8). This suggests that energy restriction has an immediate effect on the amount of released glutamate. This is not surprising given that vesicle filling, docking and replenishment are energy-costly processes.[7] An alternative explanation may be an initial hyperpolarization as described for anoxic depolarizations.[62] However, using GCaMP6f imaging we found no disruption of synchronous Ca^{2+} activity before turning into high frequency Ca^{2+} influx and intracellular Ca^{2+} loading. Oscillatory behavior like this has also been described for the onset of anoxic depolarizations,[63] where network desynchronization may occur and above-threshold depolarization can cause short periods of cell autonomous high-frequency firing, (e.g.,[51]; Figure S6) before ion gradients deteriorate and firing is lost.

Our 2–5 min chemical ischemia protocol was short enough to allow for recovery of synchronous activity in all slices (Figures 1 and S8). Post-ischemic glutamate transients showed increased decay times, yet a bias due to lower signal intensities cannot be excluded. However, also post-ischemic Ca^{2+} events, despite having similar signal intensity, showed increased decay times, which indicates that the chemical ischemia protocol might

Figure 6. Plumes become more frequent and pronounced during chemical ischemia and are associated with "defect" regions

(A) Glutamate accumulation during chemical ischemia. Scale bar: 200 μm.

(B) ΔF/F trace of the responding region.

(C) Localization and size of plumes (white circles, full-width) in different time windows during the "rise" of glutamate accumulation and "decay" period. The glutamate accumulation is shown in the background (minimum intensity projections, 5 s each). In addition, the respective plume frequency is given. The analyzed time windows are indicated on the right. See also Figure S21. Scale bar: 200 μm.

(D) Plume frequency. Individual data points are shown in light colors, means in dark, and SD as shaded areas.

(E and F) Plume size and duration (see also Figure S22). Numbers in parentheses give the number of analyzed plumes. Boxes show medians and 25–75% percentiles, red bars indicate the mean. Mann-Whitney U tests were used for pairwise comparison of individual time windows to control (ctrl; gray cf. Figure S14), Kruskal-Wallis tests were used to test for differences between the six different time windows, followed by Dunn's test (purple). ns not significant, $^*p < 0.05$, $^{**}p < 0.01$, $^{***}p < 0.001$.

(G) Example of a slice that showed high baseline intensity and glutamate fluctuations after culturing. Unusually large and frequent plumes were observed in the vicinity of these "defunct" regions. Scale bar: 200 μm.

(H) Regions with high plume-incidence acted as nuclei for ischemic glutamate accumulation. Shown are ΔF/F maximal intensity projections (MIP) of different time windows (10 s or longer periods on the right). See also Figure S23. Scale bar: 200 μm.

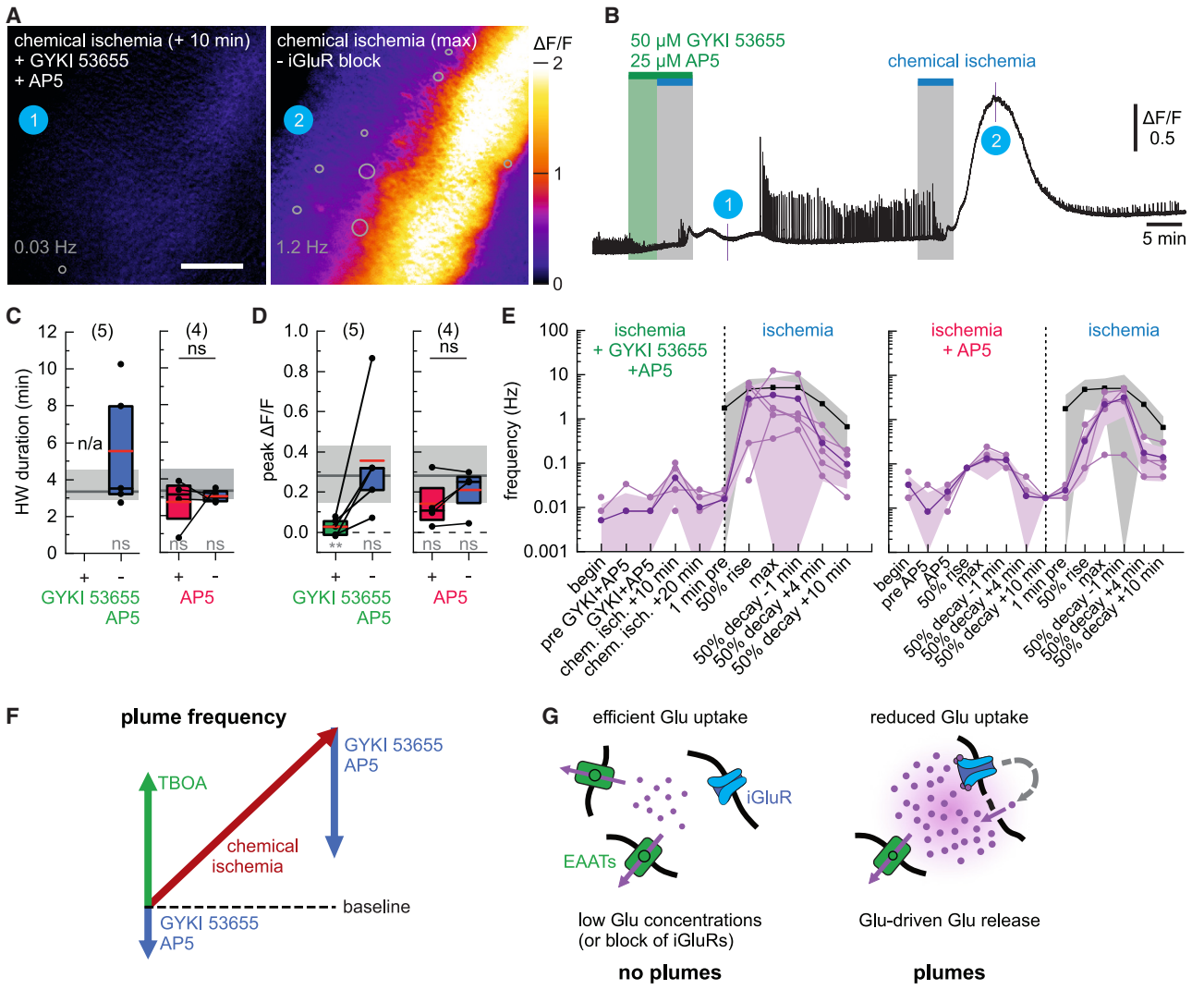

Figure 7. Chemical ischemia in the presence of iGluR inhibitors and graphical summary

(A) SF-iGluSnFR signal change upon inducing chemical ischemia in the presence of iGluR inhibitors (50 µM GYKI 53655 and 25 µM D-AP5; left) followed by a 2nd chemical ischemia without inhibitors (right). Minimum intensity projections (25 s) of glutamate accumulation with plume localization (circles; full-width) and plume frequencies. Scale bar: 200 µm.

(B) Corresponding ΔF/F trace.

(C) Half-width duration of ischemic glutamate accumulation in the presence of blockers (GYKI 53655 + AP5 ($n = 5$ slices) or just AP5 ($n = 4$ slices)) and after washout. Boxes show medians and 25–75% percentiles, red bars indicate the mean. Mann-Whitney U tests were used for pairwise comparison to control (gray, cf. Figure 1G) and comparison with and after using blockers (black); ns not significant, $^{*}p < 0.05$, $^{**}p < 0.01$.

(D) Peak ΔF/F of the observed glutamate accumulations. Data representation and statistics as in (C).

(E) Plume frequencies at the indicated time points (purple). Individual data points are shown in light colors, means in dark, and SD as shaded areas. The black/gray curves show the data of previous chemical ischemia experiments (cf. Figure 6D).

(F) Summary of observed plume frequency changes: The number of plumes was low in baseline conditions, but increased upon blocking glutamate uptake with TBOA, and it was reduced upon inhibiting iGluRs with GYKI 53655 and/or AP5. Chemical ischemia caused a strong increase in plume frequency, which was strongly reduced by adding GYKI 53655 and AP5.

(G) Model: plume formation seems to be at least partially driven by elevated extracellular glutamate concentrations and iGluRs, i.e., by an "auto-catalytic" recruitment of additional glutamate sources.

have caused some persisting effects, e.g., extracellular space changes due to cell swelling[43,64] and/or impairment of astrocyte function.[65–67] During recovery, synchronous Ca^{2+} events showed another high-frequency period, around the time when the first glutamate events began to reappear. Apparently, network activity resumed, although the amount of released glutamate had not reached normal levels yet. SF-iGluSnFR variants with higher affinity or improved synaptic localization[27,68] may provide higher sensitivity to capture these processes in more detail.

Plumes are atypical glutamate release events which are rarely seen under normal conditions

Besides synchronous activity, SF-iGluSnFR(A184V) widefield imaging revealed locally confined yet heterogeneous glutamate release events. We refer to these events as ''plumes'', which reflects their spontaneous occurrence, slow kinetics and relatively large size (Figures 2 and 3). This term was recently introduced by Parker et al.,[31,69] who observed a similar phenomenon in 2-photon *in vivo* imaging experiments in a familial hemiplegic migraine type 2 (FHM2) mouse model with reduced astrocytic Na^+/K^+-ATPase function.

Glutamate plumes showed remarkable features. Plumes were not correlated with network activity but occurred locally and randomly. In line with this, the plume frequency was not strongly decreased, when we suppressed network activity with TTX (Figures 4A, 4B, and S15), nor did it increase, when we strengthened network activity by adding gabazine (Figure S16). Plumes occurred in the presence of TTX, i.e., they did not require Na_v channel activation, which distinguishes them from action potential-driven synaptic glutamate release. Also, the heterogeneity of plumes, their relatively large size (FWHM 17.2 ± 6.4 μm) and long duration (several hundred milliseconds) sets them apart from synaptic release events. The slow kinetics of plumes are particularly striking. Plumes decayed more slowly than the transients associated with synchronous network activity, although the latter had higher overall signal amplitudes and report on synchronous and bursting release from thousands of synapses across the whole slice. Also published measurements of evoked release with various iGluSnFR variants show much faster decay kinetics than plumes.[19–21,23,26] Spontaneous release events[68] or miniature events, which are also TTX-insensitive, give rise to even faster iGluSnFR signals.[27,70]

The amount of glutamate that is released in individual plumes is hard to estimate, since SF-iGluSnFR(A184V) is a non-ratiometric sensor, the resolution in *z* dimension was limited, and glutamate calibrations were difficult to perform *in situ* (Figure S4). However, based on the affinity of SF-iGluSnFR(A184V) (reported EC_{50} = 2.1 μM),[19] it seems likely that during plumes the glutamate concentration reached hundred nanomolar to low micromolar concentrations. Given the large size and slow decay of plumes, it seems unlikely that this amount of glutamate originates from single sources, such as synaptic boutons of individual neurons. More quantitative insight might be provided by measurements with additional low-affinity SF-iGluSnFR variants, imaging with higher spatial resolution, or modeling, also taking glutamate buffering by SF-iGluSnFR into account.[71] In any case, we presume that plumes either originate from very large individual glutamate sources like astrocytes and/or multiple cells within a region, possibly linked by a feedforward mechanism.

Support for a feedforward mechanism comes from our experiments, in which we artificially increased the glutamate levels by blocking glutamate uptake. When we used TFB-TBOA to block EAAT1-3, the plume frequency increased 6- up to 73-fold (Figures 5B and S17). Besides this, TFB-TBOA caused a sustained 1.4-fold increase in the mean plume size, whereas plume half-width duration, decay time and intensity (ΔF/F) remained unaffected. The fact that TFB-TBOA had a direct effect on plume frequency but less on plume characteristics indicates that increased glutamate concentrations are important for plume induction/formation (Figures 7F and 7G), whereas EAAT function appears to be less relevant for plume termination and dissipation/removal of the released glutamate.

Last, the number of plumes was rapidly reduced upon inhibiting iGluRs, namely AMPA and NMDA receptors, by adding GYKI 53655 and D-AP5, respectively (Figures 5E–5G). This supports the findings obtained with TFB-TBOA and suggests that glutamate itself is a key driver for plume formation by activating iGluRs (Figures 7F and 7G). Once more, this distinguishes plumes from miniature release events, which should be insensitive to iGluR block. When we just blocked NMDA receptors, which are activated by low micromolar glutamate concentrations,[2] with D-AP5 we found a partial reduction in plume frequency (Figure 5I), which suggests that also AMPA receptors and possible also mGluRs contribute to plume induction. This might also explain why Parker et al. found no frequency reduction of glutamate plumes in FHM2 mice, where the glutamate concentrations might be even higher.[31]

It should be noted that plumes were observed under baseline conditions, albeit rarely. The observed frequencies were low and varied between slices (Figure S12), and a substantial fraction of slices showed no plumes. In general, low iGluSnFR expression densities could limit the capability to detect plumes.

Parker et al., who performed 2-photon *in vivo* imaging experiments reported that plumes were mostly absent in wild-type animals but detected plumes in FHM2 mice, mostly in superficial cortical layer 1, but also layer 2/3.[31] They further showed that the occurrence of plumes was related to a reduced number of astrocytes and EAAT2 (GLT-1) expression in these regions. Similarly, our organotypic slice cultures may not fully recapitulate the situation encountered in healthy brain tissue *in vivo*. For instance, reactive astrocytes, which may have reduced glutamate uptake capacity, can be overly present in slice cultures, mainly on the surface.[72–74]

Parker et al. suggested that plumes depend on vesicular release from neurons,[31] but further investigations seem warranted. We here did not test the effect of Ni^{2+}, since it is a broad ion channel blocker that also inhibits iGluRs, which we found to be important for plume induction. Also with other pharmacological manipulations, such as increasing cytosolic Ca^{2+} levels or blocking endocytosis/exocytosis altogether, it is difficult to exclude indirect effects and it is also impossible to dissect the contributions of astrocytes and neurons. Whether occasional cytosolic Ca^{2+} elevations are related to plumes remains to be investigated.

Besides activity-dependent vesicular release from the presynapse, other glutamate release mechanisms have been described, such as vesicular glutamate release from astrocytes/glia,[75–77] or release through other channels, such as P2X receptors, bestrophin-1 (Best1), or Swell1.[78,79] Notably, even when EAATs are blocked with TBOA, glutamate maintains to have a strongly depolarizing effect on astrocytes through NMDA receptor activation and elevated extracellular K^+ concentrations.[80] Plume-like release events may also be seen for other neurotransmitters, e.g., local, yet slow, ATP release events were recently observed in neuron-glia co-cultures and in mouse cortex upon inducing inflammation.[81]

Plumes contribute to glutamate accumulation during chemical ischemia

Chemical ischemia caused a strong increase in plume frequency (Figure 6D) and also plume size, signal intensity, duration, and decay times were significantly increased (Figures 6E, 6F, and S22). As such, energy depletion elicited far stronger effects than just blocking glutamate uptake with TFB-TBOA. This is not surprising since ATP depletion does not only reduce glutamate uptake but also disrupts many other aspects of neuronal and astrocytic homeostasis, eventually also resulting in pronounced extracellular glutamate accumulation (Figure 1).

However, it appears that plumes were a main source of extracellular glutamate accumulation in our chemical ischemia experiments. Synchronous glutamate release had already ceased at this time (Figure 1E) and regions with high plume activity were the first to reach plateauing signals, which most likely reflect sensor saturation (Figure 6). Plumes reappeared in these regions, as soon as the extracellular glutamate concentration began to drop in the recovery phase. At the edges of these saturated regions, plumes were visible throughout the ischemic period. Apparently, plumes persisted throughout energy depletion, which indicates that the underlying release mechanisms are not strongly reliant on continuous energy supply. At later stages the plume frequency normalized, but plume sizes and durations remained increased compared to pre-ischemic conditions, which again points to some persistent changes, as described earlier for synchronous activity.

Another link between plumes and glutamate accumulation was found in slices with defect regions. There the defect regions clearly served as nuclei for further glutamate accumulation (Figure 6G).

Quite strikingly, the presence of GYKI 53655 and D-AP5, suppressed the occurrence of plumes as well as ischemic glutamate accumulation (Figure 7). Just blocking NMDA receptors with D-AP5 had again a partial effect on plumes and some glutamate accumulation was seen (Figures 7C–7E). Overall, this experiment demonstrates that glutamate itself plays a driving role for glutamate accumulation in the acute ischemic phase and it further supports the impression that plume-like events are a major contributor to this accumulation.

Glutamate plumes may have broader pathological significance

Glutamate accumulation has long been considered to be a key factor in ischemia and cortical spreading depolarizations (SDs),[12,16,60] the latter also occurring in the context of brain injuries, migraine, and epilepsy. Indeed, previous *in vivo* SF-iGluSnFR measurements demonstrated wave-like glutamate accumulations after SD induction through focal KCl application.[29,30] In our case, the whole tissue is energy deprived, which results in a slower and more sustained glutamate accumulation with properties more similar to anoxic depolarizations.[62,82] Still, Parker et al. observed glutamate plumes also upon inducing SDs, where plumes were observed at the initiation site before SD onset and again in the decaying glutamate wavefront.[31] However, it should be noted that it remains debated how much elevated extracellular glutamate levels contribute to SD initiation and spreading, also in comparison to extracellular K^+ waves, cellular depolarization, and Ca^{2+} elevations.[16,60]

Our data indicate that increased extracellular glutamate concentrations can trigger more glutamate release, specifically, in the form of plume-like events. We further found that this mechanism operates under energy-scarce conditions and in the absence of network function. It thus has the ability to mediate large-scale glutamate accumulation in the acute phase of metabolic stress.

Plumes may also occur in the context of more subtle disbalances in glutamate homeostasis. In our slice cultures, plumes were even observed under baseline conditions but also in FHM2 mice.[31] Plumes could become significant as soon as glutamate uptake becomes suboptimal, e.g., due to transporter malfunction, increased metabolic demands, reduced astrocyte function, or reduced neurovascular coupling.[83] Reduced glutamate uptake, for instance, has been observed in the context of Alzheimer's disease, where, in a mouse model, Aβ plaques caused a local reduction of EAATs that slowed glutamate uptake and enhanced transients after evoked glutamate release[35] (see also the studies by Zott B. et al.[36] and Brymer K.J. et al.[37]). Notably, Hefendehl et al. also reported increased glutamate baseline fluctuations around Aβ plaques,[35] which are reminiscent of the plume-like activity we observed around defect regions (Figure 6G). Reduced glutamate uptake capacity has also been reported for a model of Huntington's disease[40] and might occur with age, as brain integrity becomes compromised. Besides glutamate uptake pathologies, also glutamate release may be increased (glutamatergic hyperactivity), e.g., in Parkinson's disease or inflammations.[84]

Limitations of the study

We here provide a rather phenomenological description of plume-like glutamate release events, which become more pronounced under energy scarce conditions. We found that reduced glutamate uptake and iGluR activation play important roles in triggering plumes, but the cellular sources and release mechanisms causing plumes remain to be identified. At present it is questionable, whether plumes would also occur in healthy, intact brain tissue. Due to experimental limitations of imaging with fluorescent sensors we cannot provide estimates of how much glutamate is released as part of individual plume-like events. Individual plumes could interfere with synaptic function or they may not have any direct effects at all. We also did not test how the occurrence of glutamate plumes is related to tissue depolarization or changes in intracellular Ca^{2+} concentrations. However, plumes appear to be a main contributing factor to glutamate accumulation in metabolic stress conditions, i.e., chemical ischemia in cortical slice cultures from mice, but also other release mechanisms may contribute. In summary, further research on the occurrence and relevance of plumes is warranted in other experimental paradigms. Whether plumes could play a role for neurological diseases in humans, remains to be demonstrated.

RESOURCE AVAILABILITY

Lead contact

Requests for further information and resources should be directed to and will be fulfilled by the lead contact, Andreas Reiner (andreas.reiner@rub.de).

Materials availability

This study did not generate new unique reagents.

Data and code availability

- All data reported in this paper will be shared by the lead contact upon request.
- All original code (simulations) can be found at https://gitlab.utwente.nl/m7686441/focalglutamate_modelsimulations.
- Any additional information required to reanalyze the data reported in this paper is available from the lead contact upon request.

ACKNOWLEDGMENTS

We thank the staff of the animal facility and Silvia Schweer for technical assistance at Ruhr University Bochum. Tatjana Surdin, Stefan Herlitze, and Melanie Mark (Ruhr University Bochum) provided advice on rAAV production. Nina Dietzel contributed to SF-iGluSnFR pH control measurements. We also thank Claudia Roderigo and Simone Durry for technical assistance at Heinrich Heine University. Last we thank all members of the DFG Research Unit 2795 "*Synapses under stress*", which provided the framework for this project. This work was in part supported by the NRW-Rückkehrprogramm and the DFG RU 2795 "*Synapses under stress*" with grants to A.R. (DFG RE 3101/3-1) and C.R.R. (DFG RO 2327/13-2 and 14-2).

AUTHOR CONTRIBUTIONS

T.Z. and A.R. designed the overall project; T.Z. and J.S.E.N. established organotypic slice cultures at RUB; T.Z. conducted all glutamate and Ca^{2+} imaging experiments and analyzed them with A.R.; N.P. performed ATP imaging experiments at HHU that were designed and supervised by C.R.R.; F.I.M.v.A., M.K., and H.G.E.M. performed simulations; A.R. and T.Z. wrote the manuscript with input from all authors.

DECLARATION OF INTERESTS

The authors declare no competing interests.

STAR★METHODS

Detailed methods are provided in the online version of this paper and include the following:

- KEY RESOURCES TABLE
- EXPERIMENTAL MODEL AND STUDY PARTICIPANT DETAILS
- METHOD DETAILS
  - Preparation of rAAV particles
  - Preparation of organotypic slice cultures and transduction with rAAVs
  - Imaging, chemical ischemia and pharmacological manipulations
  - ATP measurements (ATeam imaging)
  - SF-iGluSnFR(A148V) control experiments in HEK cells
  - Computational modeling of transient chemical ischemia
- QUANTIFICATION AND STATISTICAL ANALYSIS
  - Image analysis and plume identification
  - Quantification and figure representations
  - Supplementary movies
  - Statistics
- ADDITIONAL RESOURCES

SUPPLEMENTAL INFORMATION

Supplemental information can be found online at https://doi.org/10.1016/j.isci.2025.112256.

Received: May 15, 2024
Revised: December 2, 2024
Accepted: March 17, 2025
Published: March 20, 2025

REFERENCES

1. Rusakov, D.A., and Stewart, M.G. (2021). Synaptic environment and extrasynaptic glutamate signals: The quest continues. Neuropharmacology *195*, 108688. https://doi.org/10.1016/j.neuropharm.2021.108688.
2. Reiner, A., and Levitz, J. (2018). Glutamatergic signaling in the central nervous system: Ionotropic and metabotropic receptors in concert. Neuron *98*, 1080–1098. https://doi.org/10.1016/j.neuron.2018.05.018.
3. Rose, C.R., Felix, L., Zeug, A., Dietrich, D., Reiner, A., and Henneberger, C. (2017). Astroglial glutamate signaling and uptake in the hippocampus. Front. Mol. Neurosci. *10*, 451. https://doi.org/10.3389/fnmol.2017.00451.
4. Danbolt, N.C., Furness, D.N., and Zhou, Y. (2016). Neuronal vs glial glutamate uptake: Resolving the conundrum. Neurochem. Int. *98*, 29–45. https://doi.org/10.1016/j.neuint.2016.05.009.
5. Rodríguez-Campuzano, A.G., and Ortega, A. (2021). Glutamate transporters: Critical components of glutamatergic transmission. Neuropharmacology *192*, 108602. https://doi.org/10.1016/j.neuropharm.2021.108602.
6. Andersen, J.V., Markussen, K.H., Jakobsen, E., Schousboe, A., Waagepetersen, H.S., Rosenberg, P.A., and Aldana, B.I. (2021). Glutamate metabolism and recycling at the excitatory synapse in health and neurodegeneration. Neuropharmacology *196*, 108719. https://doi.org/10.1016/j.neuropharm.2021.108719.
7. Attwell, D., and Laughlin, S.B. (2001). An energy budget for signaling in the grey matter of the brain. J. Cerebr. Blood Flow Metabol. *21*, 1133–1145. https://doi.org/10.1097/00004647-200110000-00001.
8. Choi, D.W. (2020). Excitotoxicity: Still hammering the ischemic brain in 2020. Front. Neurosci. *14*, 579953. https://doi.org/10.3389/fnins.2020.579953.
9. Belov Kirdajova, D., Kriska, J., Tureckova, J., and Anderova, M. (2020). Ischemia-triggered glutamate excitotoxicity from the perspective of glial cells. Front. Cell. Neurosci. *14*, 51. https://doi.org/10.3389/fncel.2020.00051.
10. Armada-Moreira, A., Gomes, J.I., Pina, C.C., Savchak, O.K., Gonçalves-Ribeiro, J., Rei, N., Pinto, S., Morais, T.P., Martins, R.S., Ribeiro, F.F., et al. (2020). Going the extra (synaptic) mile: Excitotoxicity as the road toward neurodegenerative diseases. Front. Cell. Neurosci. *14*, 90. https://doi.org/10.3389/fncel.2020.00090.
11. Dirnagl, U., Iadecola, C., and Moskowitz, M.A. (1999). Pathobiology of ischaemic stroke: An integrated view. Trends Neurosci. *22*, 391–397. https://doi.org/10.1016/S0166-2236(99)01401-0.
12. Dreier, J.P., and Reiffurth, C. (2015). The stroke-migraine depolarization continuum. Neuron *86*, 902–922. https://doi.org/10.1016/J.NEURON.2015.04.004.
13. Passlick, S., Rose, C.R., Petzold, G.C., and Henneberger, C. (2021). Disruption of glutamate transport and homeostasis by acute metabolic stress. Front. Cell. Neurosci. *15*, 637784. https://doi.org/10.3389/fncel.2021.637784.
14. Ge, Y., Chen, W., Axerio-Cilies, P., and Wang, Y.T. (2020). NMDARs in cell survival and death: Implications in stroke pathogenesis and treatment. Trends Mol. Med. *26*, 533–551. https://doi.org/10.1016/j.molmed.2020.03.001.
15. Yu, S.P., Jiang, M.Q., Shim, S.S., Pourkhodadad, S., and Wei, L. (2023). Extrasynaptic NMDA receptors in acute and chronic excitotoxicity: Implications for preventive treatments of ischemic stroke and late-onset Alzheimer's disease. Mol. Neurodegener. *18*, 43. https://doi.org/10.1186/s13024-023-00636-1.
16. Andrew, R.D., Farkas, E., Hartings, J.A., Brennan, K.C., Herreras, O., Müller, M., Kirov, S.A., Ayata, C., Ollen-Bittle, N., Reiffurth, C., et al. (2022). Questioning glutamate excitotoxicity in acute brain damage: The importance of spreading depolarization. Neurocritical Care *37*, 11–30. https://doi.org/10.1007/s12028-021-01429-4.

17. Wu, Z., Lin, D., and Li, Y. (2022). Pushing the frontiers: Tools for monitoring neurotransmitters and neuromodulators. Nat. Rev. Neurosci. *23*, 257–274. https://doi.org/10.1038/s41583-022-00577-6.

18. Marvin, J.S., Borghuis, B.G., Tian, L., Cichon, J., Harnett, M.T., Akerboom, J., Gordus, A., Renninger, S.L., Chen, T.W., Bargmann, C.I., et al. (2013). An optimized fluorescent probe for visualizing glutamate neurotransmission. Nat. Methods *10*, 162–170. https://doi.org/10.1038/nmeth.2333.

19. Marvin, J.S., Scholl, B., Wilson, D.E., Podgorski, K., Kazemipour, A., Müller, J.A., Schoch, S., Quiroz, F.J.U., Rebola, N., Bao, H., et al. (2018). Stability, affinity, and chromatic variants of the glutamate sensor iGluSnFR. Nat. Methods *15*, 936–939. https://doi.org/10.1038/s41592-018-0171-3.

20. Armbruster, M., Hanson, E., and Dulla, C.G. (2016). Glutamate clearance is locally modulated by presynaptic neuronal activity in the cerebral cortex. J. Neurosci. *36*, 10404–10415. https://doi.org/10.1523/JNEUROSCI.2066-16.2016.

21. Helassa, N., Dürst, C.D., Coates, C., Kerruth, S., Arif, U., Schulze, C., Wiegert, J.S., Geeves, M., Oertner, T.G., and Török, K. (2018). Ultrafast glutamate sensors resolve high-frequency release at Schaffer collateral synapses. Proc. Natl. Acad. Sci. USA *115*, 5594–5599. https://doi.org/10.1073/pnas.1720648115.

22. Franke, K., Berens, P., Schubert, T., Bethge, M., Euler, T., and Baden, T. (2017). Inhibition decorrelates visual feature representations in the inner retina. Nature *542*, 439–444. https://doi.org/10.1038/nature21394.

23. Jensen, T.P., Zheng, K., Cole, N., Marvin, J.S., Looger, L.L., and Rusakov, D.A. (2019). Multiplex imaging relates quantal glutamate release to presynaptic $Ca2^{+}$ homeostasis at multiple synapses in situ. Nat. Commun. *10*, 1414. https://doi.org/10.1038/s41467-019-09216-8.

24. Barnes, J.R., Mukherjee, B., Rogers, B.C., Nafar, F., Gosse, M., and Parsons, M.P. (2020). The relationship between glutamate dynamics and activity-dependent synaptic plasticity. J. Neurosci. *40*, 2793–2807. https://doi.org/10.1523/JNEUROSCI.1655-19.2020.

25. Herde, M.K., Bohmbach, K., Domingos, C., Vana, N., Komorowska-Müller, J.A., Passlick, S., Schwarz, I., Jackson, C.J., Dietrich, D., Schwarz, M.K., and Henneberger, C. (2020). Local efficacy of glutamate uptake decreases with synapse size. Cell Rep. *32*, 108182. https://doi.org/10.1016/j.celrep.2020.108182.

26. Matthews, E.A., Sun, W., McMahon, S.M., Doengi, M., Halka, L., Anders, S., Müller, J.A., Steinlein, P., Vana, N.S., van Dyk, G., et al. (2022). Optical analysis of glutamate spread in the neuropil. Cerebr. Cortex *32*, 3669–3689. https://doi.org/10.1093/cercor/bhab440.

27. Aggarwal, A., Liu, R., Chen, Y., Ralowicz, A.J., Bergerson, S.J., Tomaska, F., Mohar, B., Hanson, T.L., Hasseman, J.P., Reep, D., et al. (2023). Glutamate indicators with improved activation kinetics and localization for imaging synaptic transmission. Nat. Methods *20*, 925–934. https://doi.org/10.1038/s41592-023-01863-6.

28. Brymer, K.J., Barnes, J.R., and Parsons, M.P. (2021). Entering a new era of quantifying glutamate clearance in health and disease. J. Neurosci. Res. *99*, 1598–1617. https://doi.org/10.1002/jnr.24810.

29. Enger, R., Tang, W., Vindedal, G.F., Jensen, V., Johannes Helm, P., Sprengel, R., Looger, L.L., and Nagelhus, E.A. (2015). Dynamics of ionic shifts in cortical spreading depression. Cerebr. Cortex *25*, 4469–4476. https://doi.org/10.1093/cercor/bhv054.

30. Rakers, C., Schmid, M., and Petzold, G.C. (2017). TRPV4 channels contribute to calcium transients in astrocytes and neurons during peri-infarct depolarizations in a stroke model. Glia *65*, 1550–1561. https://doi.org/10.1002/glia.23183.

31. Parker, P.D., Suryavanshi, P., Melone, M., Sawant-Pokam, P.A., Reinhart, K.M., Kaufmann, D., Theriot, J.J., Pugliese, A., Conti, F., Shuttleworth, C.W., et al. (2021). Non-canonical glutamate signaling in a genetic model of migraine with aura. Neuron *109*, 611–628.e8. https://doi.org/10.1016/j.neuron.2020.11.018.

32. Diaz Verdugo, C., Myren-Svelstad, S., Aydin, E., Van Hoeymissen, E., Deneubourg, C., Vanderhaeghe, S., Vancraeynest, J., Pelgrims, R., Cosacak, M.I., Muto, A., et al. (2019). Glia-neuron interactions underlie state transitions to generalized seizures. Nat. Commun. *10*, 3830. https://doi.org/10.1038/s41467-019-11739-z.

33. Shimoda, Y., Leite, M., Graham, R.T., Marvin, J.S., Hasseman, J., Kolb, I., Looger, L.L., Magloire, V., and Kullmann, D.M. (2024). Extracellular glutamate and GABA transients at the transition from interictal spiking to seizures. Brain *147*, 1011–1024. https://doi.org/10.1093/brain/awad336.

34. McGirr, A., LeDue, J., Chan, A.W., Xie, Y., and Murphy, T.H. (2017). Cortical functional hyperconnectivity in a mouse model of depression and selective network effects of ketamine. Brain *140*, 2210–2225. https://doi.org/10.1093/brain/awx142.

35. Hefendehl, J.K., LeDue, J., Ko, R.W.Y., Mahler, J., Murphy, T.H., and MacVicar, B.A. (2016). Mapping synaptic glutamate transporter dysfunction in vivo to regions surrounding Aβ plaques by iGluSnFR two-photon imaging. Nat. Commun. *7*, 13441. https://doi.org/10.1038/ncomms13441.

36. Zott, B., Simon, M.M., Hong, W., Unger, F., Chen-Engerer, H.-J., Frosch, M.P., Sakmann, B., Walsh, D.M., and Konnerth, A. (2019). A vicious cycle of β amyloid–dependent neuronal hyperactivation. Science *365*, 559–565. https://doi.org/10.1126/science.aay0198.

37. Brymer, K.J., Hurley, E.P., Barron, J.C., Mukherjee, B., Barnes, J.R., Nafar, F., and Parsons, M.P. (2023). Asymmetric dysregulation of glutamate dynamics across the synaptic cleft in a mouse model of Alzheimer's disease. Acta Neuropathol. Commun. *11*, 27. https://doi.org/10.1186/s40478-023-01524-x.

38. Parsons, M.P., Vanni, M.P., Woodard, C.L., Kang, R., Murphy, T.H., and Raymond, L.A. (2016). Real-time imaging of glutamate clearance reveals normal striatal uptake in Huntington disease mouse models. Nat. Commun. *7*, 11251. https://doi.org/10.1038/ncomms11251.

39. Koch, E.T., Woodard, C.L., and Raymond, L.A. (2018). Direct assessment of presynaptic modulation of cortico-striatal glutamate release in a Huntington's disease mouse model. J. Neurophysiol. *120*, 3077–3084. https://doi.org/10.1152/JN.00638.2018.

40. Dvorzhak, A., Helassa, N., Török, K., Schmitz, D., and Grantyn, R. (2019). Single synapse indicators of impaired glutamate clearance derived from fast iGluu imaging of cortical afferents in the striatum of normal and huntington (Q175) mice. J. Neurosci. *39*, 3970–3982. https://doi.org/10.1523/JNEUROSCI.2865-18.2019.

41. Lerchundi, R., Kafitz, K.W., Winkler, U., Färfers, M., Hirrlinger, J., and Rose, C.R. (2019). FRET-based imaging of intracellular ATP in organotypic brain slices. J. Neurosci. Res. *97*, 933–945. https://doi.org/10.1002/JNR.24361.

42. Eitelmann, S., Stephan, J., Everaerts, K., Durry, S., Pape, N., Gerkau, N.J., and Rose, C.R. (2022). Changes in astroglial K^{+} upon brief periods of energy deprivation in the mouse neocortex. Int. J. Mol. Sci. *23*, 4836. https://doi.org/10.3390/ijms23094836.

43. Meyer, J., Gerkau, N.J., Kafitz, K.W., Patting, M., Jolmes, F., Henneberger, C., and Rose, C.R. (2022). Rapid fluorescence lifetime imaging reveals that TRPV4 channels promote dysregulation of neuronal Na^{+} in ischemia. J. Neurosci. *42*, 552–566. https://doi.org/10.1523/JNEUROSCI.0819-21.2021.

44. Pape, N., and Rose, C.R. (2023). Activation of TRPV4 channels promotes the loss of cellular ATP in organotypic slices of the mouse neocortex exposed to chemical ischemia. J. Physiol. *601*, 2975–2990. https://doi.org/10.1113/JP284430.

45. Johnson, H.A., and Buonomano, D.V. (2007). Development and plasticity of spontaneous activity and up states in cortical organotypic slices. J. Neurosci. *27*, 5915–5925. https://doi.org/10.1523/JNEUROSCI.0447-07.2007.

46. Okamoto, K., Ishikawa, T., Abe, R., Ishikawa, D., Kobayashi, C., Mizunuma, M., Norimoto, H., Matsuki, N., and Ikegaya, Y. (2014). Ex vivo cultured neuronal networks emit in vivo-like spontaneous activity. J. Physiol. Sci. *64*, 421–431. https://doi.org/10.1007/s12576-014-0337-4.

47. Gerkau, N.J., Rakers, C., Durry, S., Petzold, G.C., and Rose, C.R. (2018). Reverse NCX attenuates cellular sodium loading in metabolically compromised cortex. Cerebr. Cortex *28*, 4264–4280. https://doi.org/10.1093/cercor/bhx280.

48. Imamura, H., Nhat, K.P.H., Togawa, H., Saito, K., Iino, R., Kato-Yamada, Y., Nagai, T., and Noji, H. (2009). Visualization of ATP levels inside single living cells with fluorescence resonance energy transfer-based genetically encoded indicators. Proc. Natl. Acad. Sci. USA *106*, 15651–15656. https://doi.org/10.1073/pnas.0904764106.

49. Lerchundi, R., Huang, N., and Rose, C.R. (2020). Quantitative imaging of changes in astrocytic and neuronal adenosine triphosphate using two different variants of ATeam. Front. Cell. Neurosci. *14*, 80. https://doi.org/10.3389/fncel.2020.00080.

50. M Tóth, O., Menyhárt, Á., Frank, R., Hantosi, D., Farkas, E., and Bari, F. (2020). Tissue acidosis associated with ischemic stroke to guide neuroprotective drug delivery. Biology *9*, 460. https://doi.org/10.3390/biology9120460.

51. Kalia, M., Meijer, H.G.E., van Gils, S.A., van Putten, M.J.A.M., and Rose, C.R. (2021). Ion dynamics at the energy-deprived tripartite synapse. PLoS Comput. Biol. *17*, e1009019. https://doi.org/10.1371/journal.pcbi.1009019.

52. Ibata, K., Sun, Q., and Turrigiano, G.G. (2008). Rapid synaptic scaling induced by changes in postsynaptic firing. Neuron *57*, 819–826. https://doi.org/10.1016/J.NEURON.2008.02.031.

53. Bright, D.P., and Smart, T.G. (2013). Methods for recording and measuring tonic $GABA_A$ receptor-mediated inhibition. Front. Neural Circ. *7*, 193. https://doi.org/10.3389/fncir.2013.00193.

54. Mohajerani, M.H., and Cherubini, E. (2006). Role of giant depolarizing potentials in shaping synaptic currents in the developing hippocampus. Crit. Rev. Neurobiol. *18*, 13–23. https://doi.org/10.1615/CritRevNeurobiol.v18.i1-2.30.

55. Shimamoto, K., Sakai, R., Takaoka, K., Yumoto, N., Nakajima, T., Amara, S.G., and Shigeri, Y. (2004). Characterization of novel L-threo-β-benzyloxyaspartate derivatives, potent blockers of the glutamate transporters. Mol. Pharmacol. *65*, 1008–1015. https://doi.org/10.1124/MOL.65.4.1008.

56. Tsukada, S., Iino, M., Takayasu, Y., Shimamoto, K., and Ozawa, S. (2005). Effects of a novel glutamate transporter blocker, (2S, 3S)-3-{3-[4- (trifluoromethyl)benzoylamino]benzyloxy}aspartate (TFB-TBOA), on activities of hippocampal neurons. Neuropharmacology *48*, 479–491. https://doi.org/10.1016/j.neuropharm.2004.11.006.

57. Unichenko, P., Yang, J.-W., Luhmann, H.J., and Kirischuk, S. (2015). Glutamatergic system controls synchronization of spontaneous neuronal activity in the murine neonatal entorhinal cortex. Pflügers Archiv *467*, 1565–1575. https://doi.org/10.1007/s00424-014-1600-5.

58. Bleakman, D., Ballyk, B.A., Schoepp, D.D., Palmer, A.J., Bath, C.P., Sharpe, E.F., Woolley, M.L., Bufton, H.R., Kamboj, R.K., Tarnawa, I., and Lodge, D. (1996). Activity of 2,3-benzodiazepines at native rat and recombinant human glutamate receptors in vitro: Stereospecificity and selectivity profiles. Neuropharmacology *35*, 1689–1702. https://doi.org/10.1016/S0028-3908(96)00156-6.

59. Feuerbach, D., Loetscher, E., Neurdin, S., and Koller, M. (2010). Comparative pharmacology of the human NMDA-receptor subtypes R1-2A, R1-2B, R1-2C and R1-2D using an inducible expression system. Eur. J. Pharmacol. *637*, 46–54. https://doi.org/10.1016/j.ejphar.2010.04.002.

60. Pietrobon, D., and Moskowitz, M.A. (2014). Chaos and commotion in the wake of cortical spreading depression and spreading depolarizations. Nat. Rev. Neurosci. *15*, 379–393. https://doi.org/10.1038/nrn3770.

61. Dawitz, J., Kroon, T., Hjorth, J.J.J., Mansvelder, H.D., and Meredith, R.M. (2020). Distinct synchronous network activity during the second postnatal week of medial entorhinal cortex development. Front. Cell. Neurosci. *14*, 91. https://doi.org/10.3389/fncel.2020.00091.

62. Müller, M., and Somjen, G.G. (2000). Na^+ and K^+ concentrations, extra- and intracellular voltages, and the effect of TTX in hypoxic rat hippocampal slices. J. Neurophysiol. *83*, 735–745. https://doi.org/10.1152/jn.2000.83.2.735.

63. Dzhala, V., Khalilov, I., Ben-Ari, Y., and Khazipov, R. (2001). Neuronal mechanisms of the anoxia-induced network oscillations in the rat hippocampus in vitro. J. Physiol. *536*, 521–531. https://doi.org/10.1111/j.1469-7793.2001.0521c.xd.

64. Juzekaeva, E., Gainutdinov, A., Mukhtarov, M., and Khazipov, R. (2020). Reappraisal of anoxic spreading depolarization as a terminal event during oxygen–glucose deprivation in brain slices in vitro. Sci. Rep. *10*, 18970. https://doi.org/10.1038/s41598-020-75975-w.

65. Risher, W.C., Croom, D., and Kirov, S.A. (2012). Persistent astroglial swelling accompanies rapid reversible dendritic injury during stroke-induced spreading depolarizations. Glia *60*, 1709–1720. https://doi.org/10.1002/glia.22390.

66. van Putten, M.J.A.M., Fahlke, C., Kafitz, K.W., Hofmeijer, J., and Rose, C.R. (2021). Dysregulation of astrocyte ion homeostasis and its relevance for stroke-induced brain damage. Int. J. Mol. Sci. *22*, 5679. https://doi.org/10.3390/ijms22115679.

67. Eitelmann, S., Everaerts, K., Petersilie, L., Rose, C.R., and Stephan, J. (2023). $Ca2^+$-dependent rapid uncoupling of astrocytes upon brief metabolic stress. Front. Cell. Neurosci. *17*, 1151608. https://doi.org/10.3389/fncel.2023.1151608.

68. Hao, Y., Toulmé, E., König, B., Rosenmund, C., and Plested, A.J.R. (2023). Targeted sensors for glutamatergic neurotransmission. Elife *12*, e84029. https://doi.org/10.7554/eLife.84029.

69. Eikermann-Haerter, K. (2021). Neuronal plumes initiate spreading depolarization, the electrophysiologic event driving migraine and stroke. Neuron *109*, 563–565. https://doi.org/10.1016/j.neuron.2021.01.024.

70. Farsi, Z., Walde, M., Klementowicz, A.E., Paraskevopoulou, F., and Woehler, A. (2021). Single synapse glutamate imaging reveals multiple levels of release mode regulation in mammalian synapses. iScience *24*, 101909. https://doi.org/10.1016/j.isci.2020.101909.

71. Armbruster, M., Dulla, C.G., and Diamond, J.S. (2020). Effects of fluorescent glutamate indicators on neurotransmitter diffusion and uptake. Elife *9*, e54441. https://doi.org/10.7554/ELIFE.54441.

72. Benediktsson, A.M., Schachtele, S.J., Green, S.H., and Dailey, M.E. (2005). Ballistic labeling and dynamic imaging of astrocytes in organotypic hippocampal slice cultures. J. Neurosci. Methods *141*, 41–53. https://doi.org/10.1016/j.jneumeth.2004.05.013.

73. Schreiner, A.E., Berlinger, E., Langer, J., Kafitz, K.W., and Rose, C.R. (2013). Lesion-induced alterations in astrocyte glutamate transporter expression and function in the hippocampus. ISRN Neurol. *2013*, 893605. https://doi.org/10.1155/2013/893605.

74. Lerchundi, R., Kafitz, K.W., Färfers, M., Beyer, F., Huang, N., and Rose, C.R. (2019). Imaging of intracellular ATP in organotypic tissue slices of the mouse brain using the FRET-based sensor ATeam1.03^{YEMK}. J. Vis. Exp. *154*, e60294. https://doi.org/10.3791/60294.

75. Malarkey, E.B., and Parpura, V. (2008). Mechanisms of glutamate release from astrocytes. Neurochem. Int. *52*, 142–154. https://doi.org/10.1016/j.neuint.2007.06.005.

76. Hamilton, N.B., and Attwell, D. (2010). Do astrocytes really exocytose neurotransmitters? Nat. Rev. Neurosci. *11*, 227–238. https://doi.org/10.1038/nrn2803.

77. de Ceglia, R., Ledonne, A., Litvin, D.G., Lind, B.L., Carriero, G., Latagliata, E.C., Bindocci, E., Di Castro, M.A., Savtchouk, I., Vitali, I., et al. (2023). Specialized astrocytes mediate glutamatergic gliotransmission in the CNS. Nature *622*, 120–129. https://doi.org/10.1038/s41586-023-06502-w.

78. Yang, J., Vitery, M.D.C., Chen, J., Osei-Owusu, J., Chu, J., and Qiu, Z. (2019). Glutamate-releasing SWELL1 channel in astrocytes modulates synaptic transmission and promotes brain damage in stroke. Neuron *102*, 813–827.e6. https://doi.org/10.1016/J.NEURON.2019.03.029.

79. Owji, A.P., Wang, J., Kittredge, A., Clark, Z., Zhang, Y., Hendrickson, W.A., and Yang, T. (2022). Structures and gating mechanisms of human bestrophin anion channels. Nat. Commun. *13*, 3836. https://doi.org/10.1038/s41467-022-31437-7.

80. Srivastava, I., Vazquez-Juarez, E., and Lindskog, M. (2020). Reducing glutamate uptake in rat hippocampal slices enhances astrocytic membrane depolarization while down-regulating CA3–CA1 synaptic response. Front. Synaptic Neurosci. *12*, 37. https://doi.org/10.3389/fnsyn.2020.00037.

81. Wu, Z., He, K., Chen, Y., Li, H., Pan, S., Li, B., Liu, T., Xi, F., Deng, F., Wang, H., et al. (2022). A sensitive GRAB sensor for detecting extracellular ATP in vitro and in vivo. Neuron *110*, 770–782.e5. https://doi.org/10.1016/j.neuron.2021.11.027.

82. Jarvis, C.R., Anderson, T.R., and Andrew, R.D. (2001). Anoxic depolarization mediates acute damage independent of glutamate in neocortical brain slices. Cerebr. Cortex *11*, 249–259. https://doi.org/10.1093/cercor/11.3.249.

83. Tarantini, S., Tran, C.H.T., Gordon, G.R., Ungvari, Z., and Csiszar, A. (2017). Impaired neurovascular coupling in aging and Alzheimer's disease: Contribution of astrocyte dysfunction and endothelial impairment to cognitive decline. Exp. Gerontol. *94*, 52–58. https://doi.org/10.1016/j.exger.2016.11.004.

84. Campanelli, F., Natale, G., Marino, G., Ghiglieri, V., and Calabresi, P. (2022). Striatal glutamatergic hyperactivity in Parkinson's disease. Neurobiol. Dis. *168*, 105697. https://doi.org/10.1016/j.nbd.2022.105697.

85. Close, B., Banister, K., Baumans, V., Bernoth, E.-M., Bromage, N., Bunyan, J., Erhardt, W., Flecknell, P., Gregory, N., Hackbarth, H., et al. (1997). Recommendations for euthanasia of experimental animals: Part 2. Lab. Anim. *31*, 1–32. https://doi.org/10.1258/002367797780600297.

86. Chen, T.W., Wardill, T.J., Sun, Y., Pulver, S.R., Renninger, S.L., Baohan, A., Schreiter, E.R., Kerr, R.A., Orger, M.B., Jayaraman, V., et al. (2013). Ultrasensitive fluorescent proteins for imaging neuronal activity. Nature *499*, 295–300. https://doi.org/10.1038/nature12354.

87. Grieger, J.C., Choi, V.W., and Samulski, R.J. (2006). Production and characterization of adeno-associated viral vectors. Nat. Protoc. *1*, 1412–1428. https://doi.org/10.1038/nprot.2006.207.

88. Eickelbeck, D., Karapinar, R., Jack, A., Suess, S.T., Barzan, R., Azimi, Z., Surdin, T., Grömmke, M., Mark, M.D., Gerwert, K., et al. (2019). CaMello-XR enables visualization and optogenetic control of Gq/11 signals and receptor trafficking in GPCR-specific domains. Commun. Biol. *2*, 60. https://doi.org/10.1038/s42003-019-0292-y.

89. Stoppini, L., Buchs, P.-A., and Muller, D. (1991). A simple method for organotypic cultures of nervous tissue. J. Neurosci. Methods *37*, 173–182. https://doi.org/10.1016/0165-0270(91)90128-M.

90. Gee, C.E., Ohmert, I., Wiegert, J.S., and Oertner, T.G. (2017). Preparation of slice cultures from rodent hippocampus. Cold Spring Harb. Protoc. *2017*, 126–130. https://doi.org/10.1101/pdb.prot094888.

91. Edelstein, A.D., Tsuchida, M.A., Amodaj, N., Pinkard, H., Vale, R.D., and Stuurman, N. (2014). Advanced methods of microscope control using μManager software. J. Biol. Methods *1*, e10. https://doi.org/10.14440/jbm.2014.36.

92. Pollok, S., and Reiner, A. (2020). Subunit-selective iGluR antagonists can potentiate heteromeric receptor responses by blocking desensitization. Proc. Natl. Acad. Sci. USA *117*, 25851–25858. https://doi.org/10.1073/pnas.2007471117.

93. Engels, M., Kalia, M., Rahmati, S., Petersilie, L., Kovermann, P., van Putten, M.J.A.M., Rose, C.R., Meijer, H.G.E., Gensch, T., and Fahlke, C. (2021). Glial chloride homeostasis under transient ischemic stress. Front. Cell. Neurosci. *15*, 735300. https://doi.org/10.3389/fncel.2021.735300.

94. Schindelin, J., Arganda-Carreras, I., Frise, E., Kaynig, V., Longair, M., Pietzsch, T., Preibisch, S., Rueden, C., Saalfeld, S., Schmid, B., et al. (2012). Fiji: An open-source platform for biological-image analysis. Nat. Methods *9*, 676–682. https://doi.org/10.1038/nmeth.2019.

95. Wei, Y., Ullah, G., Ingram, J., and Schiff, S.J. (2014). Oxygen and seizure dynamics: II. computational modeling. J. Neurophysiol. *112*, 213–223. https://doi.org/10.1152/jn.00541.2013.

96. Breslin, K., Wade, J.J., Wong-Lin, K., Harkin, J., Flanagan, B., Van Zalinge, H., Hall, S., Walker, M., Verkhratsky, A., and McDaid, L. (2018). Potassium and sodium microdomains in thin astroglial processes: A computational model study. PLoS Comput. Biol. *14*, e1006151. https://doi.org/10.1371/journal.pcbi.1006151.

97. Flanagan, B., McDaid, L., Wade, J., Wong-Lin, K., and Harkin, J. (2018). A computational study of astrocytic glutamate influence on post-synaptic neuronal excitability. PLoS Comput. Biol. *14*, e1006040. https://doi.org/10.1371/journal.pcbi.1006040.

STAR★METHODS

KEY RESOURCES TABLE

REAGENT or RESOURCE	SOURCE	IDENTIFIER
Bacterial and virus strains		
AAV2/8.hSyn1.SF-iGluSnFR(A184V)	This paper	N/A
AAV2/8.hSyn1.GCaMP6f	This paper	N/A
AAV2/2.hSyn. ATeam1.03^{YEMK}	Viral Vector Core ETH Zürich, CH	N/A
Chemicals, peptides, and recombinant proteins		
NaCl	Sigma	S7653
KCl	Sigma	793590
NaH_2PO_4	Sigma	71500
$NaHCO_3$	Sigma	401676
$CaCl_2$	Sigma	21108
$MgCl_2$	Sigma	M2670
D-glucose	Sigma	G7528
L-glutamine	GIBCO/Life Technologies	25030-032
Insulin from bovine pancreas	Sigma	I6634
$MgSO_4$	Sigma	83266
$CaCl_2$	Fluka	21114
Ascorbic acid	Sigma	11140
Minimum Essential Medium Eagle (MEM)	Sigma	M7278
Hanks' Balanced Salt Solution (HBSS)	Sigma	H9394
Heat-inactivated (HI) Horse Serum	GIBCO/Life Technologies	26050-088 Lots: RNBG9990, 2353036
TFB-TBOA	Tocris	2532
TTX	Tocris	1078
GBZ (SR 95531)	Tocris	1262
GYKI 53655	HelloBio	HB0312
D-AP5	HelloBio	HB0225
DMEM	Sigma	D6429
Fetal Calf Serum	Sigma	F9665
Polyethyleneimine (PEI) 25.000	Sigma	408727
DNase I	Roche	11284932001
Polyethylene glycol (PEG)	Sigma	89510
Chloroform	Fisher Scientific	11408123
PBS	Sigma	806552
Experimental models: Cell lines		
HEK293Tsa	Dr. Deniz Dalkara	N/A
HEK293	RUB, Animal Physiology	N/A
Experimental models: Organisms/strains		
Mouse: CB57BL/6	Janvier	JLCO221002458
Mouse: Balb-C	Janvier	N/A
Recombinant DNA		
pAAV.hSynapsin.SF-iGluSnFR(A184V)	Marvin et al.	Addgene Plasmid #106175
pAAV.Syn.GCaMP6f.WPRE.SV40	Chen et al.	Addgene Plasmid #106175
Software and algorithms		
FIJI 1.53t	Schindelin et al.	https://imagej.net/
Micromanager 2.0	Edelstein et al.	https://micro-manager.org/

(*Continued on next page*)

Continued

REAGENT or RESOURCE	SOURCE	IDENTIFIER
Corel Draw 2018	Corel	https://www.coreldraw.com/
Origin Pro 2021	Origin Labs	https://www.originlab.com/origin/
ClampFit 11.1	Molecular Devices	https://www.moleculardevices.com/pclamp11
ProFit 7.0.19	Quantumsoft	https://quansoft.com/
Microsoft Excel 2019	Microsoft	-
Matlab 2023b	MathWorks	https://www.mathworks.com/products/new_products/release2023b.html
Other		
Millicell Standing Cell Culture Inserts, hydrophilized PTFE membrane, pore size 0.4 μm, Ø 30 mm	Millipore	PICM0RG50
NucleoBond Xtra Maxi Plus EF	Macherey-Nagel	740426

EXPERIMENTAL MODEL AND STUDY PARTICIPANT DETAILS

All experiments were carried out in strict accordance with the institutional guidelines as well as the European Community Council Directive (2010/63/EU). Mice (CB57BL/6) for post-mortem tissue removal were obtained from the Animal Facility of the Faculty of Biology and Biotechnology, Ruhr University Bochum and the Zentrale Einrichtung für Tierforschung und wissenschaftliche Tierschutzaufgaben (ZETT, Heinrich Heine University Düsseldorf) approved by the Landesamt für Natur, Umwelt und Verbraucherschutz (LANUV) according to §11 TierSchG. Animals were bred and housed under standard conditions with a 12 h light/dark cycle and food and water provided *ad libitum*. All efforts were taken to minimize animal suffering. All experiments carried out at the Heinrich Heine University Düsseldorf were communicated to and approved by the Animal Welfare Office at the Animal Care and Use Facility of the Heinrich Heine University Düsseldorf (Institutional act no. O50/05) and by the Animal Welfare Office at Ruhr University Bochum. In accordance with the recommendations of the European Commission,[85] neonatal animals (7-9 days postnatal) were killed by rapid decapitation before preparation of brain slices. Mice of both sexes were used as no sex specific differences in brain slices cultures were expected with respect to these experiments.

Human embryonic kidney 293 T-variant cells (HEKtsa) were cultured in Dulbeccos's Modified Eagle Medium (MEM) supplemented with 7% fetal calf serum at 37°C and 5% CO_2. For details on the specific passaging/plating procedures please refer to the corresponding method details sections (preparation of rAAV particles and SF-iGluSnFR(A148V) control experiments in HEK cells). Our cell line was not authenticated and not routinely tested for mycoplasma.

METHOD DETAILS

Preparation of rAAV particles

pAAV.hSynapsin.SF-iGluSnFR(A184V) was a gift from Loren Looger (Addgene plasmid #106175;[19]) and pAAV.Syn.GCaMP6f.WPRE.SV40 was a gift from Douglas Kim & GENIE Project (Addgene plasmid #100837;[86]). High-purity, endotoxin-free plasmids were prepared using the NucleoBond Xtra Maxi Plus EF kit (Macherey-Nagel).

rAAVs were produced in-house (Figure S25B).[87] For this HEK293Tsa cells with E1+ were grown in 151 cm^2 cell culture dishes with 20 ml DMEM with 7% fetal calf serum at 37°C and 5% CO_2. At 70% confluence plasmid triple transfections were performed. For this, serum-free DMEM (0.5 ml) was mixed with helper plasmid (12 μg), *trans*-plasmid (10 μg) and the respective *cis*-plasmid (6 μg) before adding polyethyleneimine (PEI) 25,000 (84 μg; 1 mg/ml stock in water) per dish. Purification of AAVs with a serotype 8 capsid was performed similar to a published protocol.[88] 72 h after transfection, cells were harvested with a cell scraper, separated from the medium by low-speed centrifugation (300 *g*, 4°C) and resuspended in 10 ml Tris-NaCl (150 mM NaCl, 50 mM Tris HCl; room temperature). Lysis was performed by six cycles of alternating freezing in dry ice/ethanol and thawing at 37°C, followed by 30 min incubation with DNase I (1.3 mg/ml) at 37°C. In parallel, virus particles were precipitated from the medium by adding 5 ml PEG-NaCl (40% w/v in 2.5 M NaCl) and continuous shaking at 4°C (~3.5 h). Both, the lysed cells and the PEG-precipitated medium were then centrifuged for 20 min at 3700 *g* and 4°C. Subsequently, the supernatant of the lysed cells was used to resuspend the pellets obtained from the PEG precipitation. After resuspension and shaking at 4°C overnight, 2.5 ml PEG-NaCl was added for at least 6 hours to precipitate the AAV particles, the suspension was centrifuged for 20 min at 3700 *g* and 4°C, and the pellet was resuspended in 10 ml HBS (140 mM NaCl, 50 mM HEPES, pH 7.3). Chloroform was added at 1:1 v/v ratio to remove impurities. After low-speed centrifugation at 370 *g* for 5 min at RT, the aqueous phase (without precipitate) was collected followed by 30 min of evaporation of residual chloroform. Then, the AAV suspension was sterile filtered twice (PES, 0.22 μm). Subsequently, 2.5 ml PEG-NaCl were added to precipitate the AAV particles overnight at 4°C. After 20 min centrifugation at 3700 *g* and 4°C, the pellet was resuspended in 80-100 μl PBS and stored at 4°C.

Preparation of organotypic slice cultures and transduction with rAAVs

Organotypic slice cultures were prepared from male and female CB57BL/6 mice on postnatal day 7-9 following a previously published protocol.[74] The animals were sacrificed by decapitation and the brain was quickly transferred to ice-cold Ringer's solution (125 mM NaCl, 2.5 mM KCl, 1.25 mM NaH_2PO_4, 26 mM $NaHCO_3$, 2 mM $CaCl_2$, 1 mM $MgCl_2$ and 20 mM D-glucose; 95% O_2 and 5% CO_2). The hemispheres were separated and a 45° parasagittal cut (see Figure S25A) was performed before cutting 250 μm slices using a vibratome (Leica VT1200; 1 mm amplitude, 0.9-1.0 mm/s, 15° angle) in ice-cold Ringer's solution. Then, the hippocampus with the adjacent cortex was excised and the slices were stored in 34°C Ringer's solution until the second hemisphere was sliced. Under sterile conditions, slices were washed five times in HBSS with minimal solution transfer. Finally, the slices were placed on membrane inserts (Millicell PICM0RG50, hydrophilized PTFE, pore size 0.4 μm) for cultivation according to Stoppini.[89,90] The slices were cultured at 37°C and 5% CO_2 in organotypic slice culture medium that consisted of 100 ml (20% final concentration) heat-inactivated horse serum and 394 ml MEM, 2.5 ml 200 mM L-glutamine, 2.9 ml 2.5 M NaCl, 0.4 ml 2.5 M $MgSO_4$, 0.72 ml 2.5 M $CaCl_2$, 2.4 μl 25% ascorbic acid and 1.16 g glucose. The resulting ion concentrations in the non-serum fraction were: 138 mM Na^+, 5.27 mM K^+, 3.29 mM Mg^{2+}, 3.13 mM Ca^{2+}, 122.1 mM Cl^- and 21.5 mM glucose. A full medium exchange was performed three to four times a week. In the first 24 h after slicing, the slices, which encompassed portions of cortex and hippocampus, showed swelling. Until DIV (day *in vitro*) 7 slices deswelled, became translucent and started to flatten, with some cells migrating outwards.

Slice cultures were transduced on DIV1 by adding 1 μl AAV particles (diluted 1:3, 1:5 or 1:7 in PBS) onto the center of the cortical region. The medium was exchanged after 24-48 h.

Imaging, chemical ischemia and pharmacological manipulations

Imaging experiments were performed at DIV 14-21. Before transfer to the microscope, slices were visually assessed for flattening of the slice and a lucid appearance. Slices with white spots, indicating necrosis, were discarded. Slices were placed in a custom-made chamber (1 ml volume) and superfused with Ringer's solution (see Preparation section) at 1-3 ml/min and 24°C using a peristaltic pump (Gilson Minipuls 3) and in-line heater, respectively. The bath solution was fully exchanged in 90 s or less. The chamber was placed under an upright microscope (Zeiss Axioscope) fitted with a 10x/0.3 water immersion objective (Zeiss N-Achroplan M27). Epifluorescence excitation was provided by a xenon light source (Sutter Instruments, Lambda DG-4) with a 470/40 nm excitation filter and a light-guide (Thorlabs, LLG3-6H), a 495 nm dichroic mirror (AHF, T495LPXR) and a 525/39 nm emission filter (Semrock, 525/39 BrightLine HC). For high-speed imaging the DG4 and light guide were replaced by a collimator-coupled LED (Thorlabs, M470L4) using the same filter set. The light intensity in the sample plane was adjusted to ~0.4 mW/mm^2. Images were acquired at 20 fps or 99 fps for glutamate imaging and at 10 fps for calcium imaging with an EMCCD camera (Photometrics, Evolve 512delta) at 16 bit in pre-sequence clearing mode with 512 x 512 or 256 x 256 pixels using MicroManager2.0.[91] At 256 pixels one pixel corresponded to 3.22 μm.

The slices were allowed to equilibrate in the experimental chamber for 15-20 min prior to imaging with constant superfusion as described above. Typically, 5 min baseline imaging was performed before blockers were added or chemical ischemia was evoked by applying an ischemic Ringer's solution (with 0 mM D-glucose, 2 mM 2-deoxyglucose and 5 mM NaN_3) for 2-5 min. For pharmacological characterization 1 μM TFB-TBOA, 0.2 μM TTX, 3 μM GBZ, 50 μM GYKI 53655 or 25 μM D-AP5 in Ringer's solution were applied for 4 min. The shown application bars are corrected for the experimentally determined 1 min dead-time. Typical ischemia or pharmacological recordings lasted up to 50 min, experiments with a second ischemia (Figure 7) up to 1.5 h. Some slices were not further imaged, if they showed no neuronal outgrowth, weak sensor expression, no synchronous activity or larger movements during the recordings.

ATP measurements (ATeam imaging)

Imaging of intracellular ATP changes in neurons was performed in layer II/III of the somatosensory cortex using the FRET-based nanosensor ATeam1.03^{YEMK} ("ATeam").[48,49] 0.5 μl of rAAV encoding for ATeam under the neuron-specific promoter human synapsin1 (hSyn1, AAV2/2) were applied on the cultured slices during the first 3 days *in vitro*.[49] The rAAV encoding for ATeam was generated at the Viral Vector Facility of the University/ETH Zürich (Switzerland). Slices were then kept in culture for at least 10 more days until experiments were performed. A confocal laser scanning microscope (Nikon Eclipse C1) equipped with a 40x Achroplan water immersion objective (Nikon, NA 0.8) was used to confirm neuron-specific expression of ATeam (Figure S1A). ATeam was excited using a 488 nm argon ion laser and fluorescence emission was collected at 515 ± 15 nm. Maximum projections were constructed from *z*-stacks (step size 1.5 μm) using Fiji (ImageJ).

Prior to experiments, the glial scar on the transduced slices was removed as described.[74] Slices were placed in a bath chamber at room temperature and were superfused at 2-2.5 ml/min with Ringer's solution (130 mM NaCl, 2.5 mM KCl, 2 mM $CaCl_2$, 1 mM $MgCl_2$, 1.25 mM NaH_2PO_4, 26 mM $NaHCO_3$ and 10 mM glucose, bubbled with 95% O_2 and 5% CO_2, resulting in a pH of 7.35). Fluorescence imaging was performed using an epifluorescence microscope (Nikon Eclipse FN-I) equipped with an 40x Achroplan water immersion objective (Nikon, NA 0.8). ATeam was excited at 434 nm using a Poly-V monochromator (Thermo Scientific/FEI) for 25-50 ms at a frequency of 0.5 Hz. Emitted light was split at 500 nm using a W-View GEMINI image splitter (Hamamatsu Photonics), band-pass filtered at 483/32 (eCFP, donor) and 542/27 (Venus, acceptor) and imaged with a sCMOS camera (Hamamatsu Photonics, Orca 4 LT Plus). Donor and acceptor fluorescence was collected from manually drawn regions of interest (ROIs) around neuronal cell bodies using the NIS-Elements software (Nikon). After background correction, the fluorescence ratio (Venus/eCFP, termed "ATeam ratio")

was calculated for each ROI. Subsequent analysis was performed using Origin 2021 software (OriginLabs). Changes in the fluorescence ratio induced by chemical ischemia were normalized to the baseline and are expressed as % change in the ATeam fluorescence ratio (Figures S1B and S1C).

SF-iGluSnFR(A148V) control experiments in HEK cells

The effect of azide and pH on SF-iGluSnFR(A148V) was tested 24-48 h after PEI-mediated transfection of HEK cells grown on plastic coverslips.[92] Fluorescence imaging (Figure S2) was performed on an inverted microscope (Leica DMi8). HEK cells were continuously perfused with extracellular solution (138 mM NaCl, 1.5 mM KCl, 1.2 mM $MgCl_2$, 2.5 mM $CaCl_2$ and 10 mM HEPES, pH 7.3 or pH 6.5) by a gravity-driven perfusion system. Epifluorescence excitation was provided by a collimator-coupled LED (Thorlabs, M470L3) with a 470/40 nm excitation filter (Chroma, ET 470/40x) and a 495 nm dichroic mirror (Chroma, T 495 LPXR). A 525/50 nm emission filter (Chroma, ET 525/50m) was used and continuous imaging with 2 fps was performed with an EMCCD camera (Photometrics, Evolve 512delta) at 16-bit 512 x 512 pixels or 256 x 256 pixels using MicroManager2.0.[91] The obtained images were processed using ImageJ 1.53t. For dose-response analysis of SF-iGluSnFR(A184V), four individual experiments at each, pH 7.3 or pH 6.5, were performed. From each recording, the fluorescence intensities from six different cells were exported and analyzed in Excel (Microsoft). F_0 was determined individually for each application to account for signal run up or bleaching, by averaging 10 frames (5 s) before glutamate application (0.2-1000 μM glutamate in extracellular solution at pH 7.3 or pH 6.5) and 10 frames after the signal had stabilized after washout. Relative fluorescence intensity changes (ΔF/F) were calculated after averaging 10 frames at the plateau of each glutamate application. The obtained ΔF/F values were normalized to the signal change obtained with 1000 μM glutamate. EC_{50} values were determined by fitting the dose-response curves with the Hill equation using ProFit (Quantumsoft) with the Levenberg-Marquardt algorithm and fixed Hill coefficient (n = 1) and $\Delta F/F_{min} = 0$. The obtained EC_{50} values (Figure S2C) were close to the reported value for SF-iGluSnFR(A184V) (reported EC_{50} = 2.1 μM).[19] The relative signal changes upon reducing to pH 6.5 were calculated with F_0 being the signal at pH 7.3 in the absence and presence of saturating glutamate (100 μM). NaN_3 (5 mM) in extracellular solution was applied for 5 min. Additional HEK cell control experiments to investigate the baseline fluorescence increase of SF-iGluSnFRA(A84V) (Figure S3) were performed on the slice setup, with the same perfusion and the same conditions as described in imaging, chemical ischemia and pharmacological manipulations also in Ringer's solution saturated with 95% O_2 and 5% CO_2, but using a sCMOS camera (Hamamatsu, Orca Flash 4.0 LT+). The light intensity was ~0.4 mW/mm^2, if not indicated otherwise (see Figure S3C). The stability of glutamate-induced ΔF/F changes was tested with 50 μM glutamate applications in Ringer's solution (Figure S3D).

Computational modeling of transient chemical ischemia

The simulations are based on a computational model of a neuron and an astrocyte in a finite extracellular space that we had previously developed for a similar experimental setup.[51,93] The previous model explained changes in Na^+, K^+ and Cl^- concentrations as well as cell volume. This model already included Ca^{2+} and glutamate, but those components were not the main focus. We adapted and used this computational model to further understand the observations reported here. The model with all compartments and active and passive transport processes is shown in Figure S5.

The following changes were included in the model: Previously, we used a finite, closed extracellular space, while in the experiments there is a continuous flow of solution, which refreshes the extracellular space surrounding the neuron and astrocyte (bath exchange). To account for this exchange, we included diffusion from the extracellular space to an external bath with constant concentrations. The extracellular space was connected to the external bath by diffusive coupling of all ions and glutamate. To model differences in exchange rate that might be seen in different regions in the slice (thicker or more dense regions *vs.* thinner or less dense regions) we choose various values for the strength of this diffusion. Further, the ATP measurements (Figure S1) gave estimates of the drop in energy that was previously unknown. Motivated by the diffusion of the bath exchange, we adopted the modelling of available oxygen as described by Wei et al.,[95] as a proxy for the available ATP as this is directly related. This model has been used in similar contexts. Specifically, the strength of the sodium potassium ATPase (NKA) pumps indirectly depends on the available extracellular oxygen, and the pumps indirectly consume oxygen, which is replenished through diffusion with the external bath. To simulate the response to chemical ischemia, we lowered the oxygen level from 100% to 10% of baseline in the external bath for four minutes, and then restored it back to 100%. The remaining 10% oxygen could account for reserve forms of energy such as lactate.

Next, there is considerable spontaneous network activity (see e.g. Figure 1), and we thus added an input ('applied current', Figure S6) to the neuron every two minutes during the entire simulation (before, during, and after ischemia). This input also gives information about neuronal excitability. Further, the GCaMP6f signals representing neuronal Ca^{2+} (see e.g. Figure 1) suggest more Ca^{2+} inflow than our model showed previously. We thus increased the voltage-gated calcium permeability ('gated Ca^{2+}') 50-fold. Finally, for glutamate we now implemented the full nonlinear expression for the EAAT current from[96] (instead of its linearization), including two limiting terms as in,[97] which limit EAAT-mediated Glu uptake if there is too little glutamate in the extracellular space, or, if loading into vesicles is saturated.

For the simulations, we used the model by Kalia et al.,[51] where also all model components i.e. those for Na^+, K^+, and Cl^-, can be found. Here we only describe the changes we made to the model, in particular for Ca^{2+} and glutamate, and how we included diffusion.

For the neuronal or astrocytic compartment (x = n, a), we have the membrane potential V_x. The expression for the EAAT current follows the model from Breslin et al.:[96]

$$J_{EAAT} = P_{EAAT,x}\,(\exp(-\beta_{EAAT}(V_x - E_{EAAT_x})) - 1),$$

where $\beta_{EAAT} = 0.0292\, mV^{-1}$, $P_{EAAT,a} = 2 * 10^{-7} \mu m^3 (ms)^{-1}$ and $P_{EAAT,n} = P_{EAAT,a}/9$ to preserve a 1:9 ratio. The reversal potential is given by:

$$E_{EAAT,x} = \frac{RT}{2F} log\left(\frac{[Na^+]_e^3 [K^+]_x [H^+]_e [Glu]_e}{[Na^+]_x^3 [K^+]_e [H^+]_x [Glu]_x}\right).$$

Free intracellular glutamate $[Glu]_n$ is transported into a depot of vesicles with a time constant τ_{rec} until this process is saturated.

The neuronal and astrocytic NKA pumps consume energy modeled directly with oxygen as in Wei et al..[95] The available extracellular oxygen $[O_2]$ changes as:

$$\frac{d[O_2]}{dt} = -\frac{\alpha_{O_2}}{F}(J_{NKA,n} + J_{NKA,a}) + \varepsilon_{O_2}([O_{2,bath}](t) - [O_2]),$$

where $\alpha_{O_2} = 0.1656\, g/mol$, $\varepsilon_{O_2} = 7.9688 * 10^{-6}\, ms^{-1}$. The baseline level we set as $[O_{2,bath}] = 58$ g/mol and to model ischemia we set $[O_{2,bath}] = 5.8$ g/mol from t=10 to t=14 minutes. The normal NKA pump current $I_{NKA,x}$ is modulated by oxygen as:

$$J_{NKA,x} = \frac{1}{1 + exp((20 - [O_2])/3)} I_{NKA,x}.$$

For completeness, we mention the active and passive calcium currents as they were not described in[51]. The calcium leak currents are given by

$$J_{Ca,L,x} = \frac{4 P_{Ca,L,x} F^2 V}{RT}\left(\frac{[Ca]_x - [Ca]_e\, exp(-2FV_x/RT)}{1 - exp(-2FV_x/RT)}\right)$$

and the gated neuronal calcium current is given by

$$J_{Ca,g,n} = \frac{4 P_{Ca,g,n} m^2 h F^2 V_n}{RT}\left(\frac{[Ca]_n - [Ca]_e\, exp(-2FV_n/RT)}{1 - exp(-2FV_n/RT)}\right).$$

For all extracellular ions and glutamate we add diffusion to the bath as:

$$\frac{dN_x}{dt} = \sum I_{ion,x} + B(N_B - N_x),$$

where we vary the diffusion strength as $B = 2*10^{-4}$, $1*10^{-3}$, $5*10^{-3}$ ms^{-1}.

As in Kalia et al.,[51] we set the volume of the neuron and astrocyte to 2.0 and 1.7 mm^3, respectively, and then choose the volume of the extracellular space so it initially had 20% of the total volume. The synaptic cleft and neuron and astrocyte compartments where glutamate and calcium reside have a fixed volume of 1 μm^3, which is much smaller and thus negligible for the total volume. The simulation code can be found at https://gitlab.utwente.nl/m7686441/focalglutamate_modelsimulations.

General properties

We investigated key components of the model by injecting currents every two minutes before we additionally induced chemical ischemia for 4 min (Figure S6). The behavior was similar to the results obtained with the previous model.[51] The neuron was excitable under baseline conditions (see membrane potential) and maintained a normal resting potential and low Na^+, Cl^- and Ca^{2+} concentrations with significant NKA activity. Inducing chemical ischemia for 4 min resulted in deterioration of all neuronal and astrocytic ion gradients within a few minutes along with strong depolarization. Neuronal excitability was lost as well as NKA activity. After restoring oxygen supply, most components returned towards baseline levels and neuronal excitability was regained. The model also shows autonomous, high-frequency neuronal activity during the onset of ischemia, namely when neuronal depolarization has crossed the firing threshold but not reached the depolarization block, yet (see also[51]).

Effect of bath coupling

When we varied the diffusion strength to the bath from weak to strong ($B = 2*10^{-4}$, $1*10^{-3}$, $5*10^{-3}$ ms^{-1}) we found that oxygen depletion in the extracellular space, i.e., the extent to which chemical ischemia was induced, did not vary (Figure S7A). Also, strong neuronal Ca^{2+} loading was seen in all conditions (Figure S7B). However, the timecourse and extent of extracellular glutamate accumulation varied from ~75 μM (maximum at low coupling strength) to ~3 μM (maximum at high coupling strength) (Figure S7C). The other model components showed overall similar behavior to the situation seen with weak bath coupling (Figure S6), but partial recovery was somewhat faster with stronger bath coupling.

QUANTIFICATION AND STATISTICAL ANALYSIS

Image analysis and plume identification

The obtained images were processed using FIJI 1.53t.[94] Movies acquired with 512 x 512 pixels were binned to 256 x 256 pixels by averaging. ΔF/F denotes relative fluorescence changes, which were calculated with F_0 as an average of 10-200 frames with no synchronous activity. Typical time windows for analysis were 500 frames with a local F_0; in cases of low frequencies, stack sizes

were increased up to 6000 frames. Subsequently, stacks were processed with the ImageJ built-in image calculator to obtain ΔF/F stacks.

Only slices with high and evenly distributed SF-iGluSnFR(A184V) baseline fluorescence across all cortical layers (>1.5-fold above the fluorescence background) and synchronous activity before and after drug applicationwere considered for analysis (an exception are the slices shown in Figures 6G, 6H, and S23E–S23J, which showed uneven SF-iGluSnFR(A184V) baseline fluorescence). On average, the brightest pixel in a given slice was only 2.90-fold brighter than the dimmest pixel (n = 56 slices), with decreasing signal intensities towards the edges of the slices. Due to these differences in the raw iGluSnFR(A184V) signal intensity and the thinning towards the slice edges, we refrained from drawing any region-specific conclusions. Since we were interested in analyzing plumes, we selected slices with baseline plume frequencies $\geq$0.12 Hz for control, TTX, GBZ, D-AP5 and GYKI 53655/D-AP5 recordings. For ischemia experiments all slices had baseline plume frequencies $\geq$0.06 Hz. Around 70% of the slices showed fewer plumes below these frequencies.

For measuring synchronous activity, as well as glutamate or Ca^{2+} accumulations, the same responding region was used. For this as single region of interest (polygon) was manually selected based on the corresponding ΔF/F projection. Synchronous events were readily identifiable by global and rather uniform fluorescence increases, i.e. they were seen for all sensor-expressing pixels and appeared without any noticeable time delay at our imaging rate of 20 fps. At 20 fps the synchronous activity remained unresolved, as the events reflect bursts of variable duration, which also reflects the corresponding decay times (see also Figure S11). For plume analysis, maximum intensity projections (MIPs) were calculated after excluding all frames with synchronous activity by setting them to zero intensity. The obtained MIPs served to identify possible plumes, which were manually confirmed in the corresponding image stack. For further analysis of each plume, a circular region of interest was manually defined at the peak frame (maximal plume intensity).

The mean ΔF/F of all regions of interest (synchronous activity or plumes) was exported as time series to ClampFit 11.1 (Molecular Devices) to analyze the traces for peak frames, max ΔF/F, half- width (HW) duration and 10-90 % rise and decay times. Excel (Microsoft) was used to calculate logarithmic values for durations and rise and decay times. Plume sizes were determined in the corresponding maximum intensity frame (full-width at half-maximum; FWHM) at the center of the plume in x- and y-direction (Figure 3A). Plumes were mostly round (Figure 3B) but the size (FWHM) was calculated as an average of the x- and y-size to account for asymmetries. Plumes were only included into the analysis, if they possessed a ΔF/F signal change of at least 2%, lasted >50 ms (HW duration) and were at least 2 × 2 pixels in size. Small or brief plumes might have escaped our detection, especially if they occurred during synchronous activity; some other plumes could not be fully analyzed, e.g. when their decay overlapped with synchronous events (on average, global synchronous events covered 3.6% of the recording time). Plumes might have been also missed during overall increasing glutamate concentrations and were not sufficiently resolved during ischemia. We only analyzed slices with dense and clear SF-iGluSnFR expression (overall fluorescence signal >1.5-fold above background, see above), as plumes might be easily missed in sparsely transduced tissue.

In all measurements, both in slice cultures and HEK cells (see Figures S3 and S9), we noted a run-up of the SF-iGluSnFR baseline intensity of ∽20-30% over 40 min continuous imaging, which was apparently accompanied by a decrease of the signal change ΔF/F. The origin of this effect is presently unclear, but it complicated our efforts to calibrate the sensor by applying defined glutamate concentrations. This also limits the reliability of the ΔF/F amplitude measurements, which often show a decrease over their 40 min time course, as also seen in control measurements (Figure S9).

Quantification and figure representations

Figure 1 and related supplementary figures

To obtain ΔF/F maps of glutamate accumulations (Figures 1C, 6A, and S23C) and Ca^{2+} accumulations during chemical ischemia, average intensity projections of 200 frames were generated at the peak of accumulation (F). The mean resulting from average intensity projections of 200 frames before and 200 frames after chemical ischemia was used for correction (F_0). For normalization of full-length traces from selected regions (Figures 1B–1J, 6B, 7B, S4A, S9A, S9B, and S23B) the intensity F_0 from the beginning of the recordings was used (average intensity projections of 10-100 frames). To create pseudo-color time traces along line regions (Figures 1D and S23B), intensity values of all pixels along a line region of interest were obtained from ΔF/F stacks, imported to ClampFit 11.1 (Molecular Devices) for manual baseline adjustments (linear segments), and visualized in Origin Pro 2021 (OriginLabs) using an inverted 'inferno' color scale.

Responding regions, i.e. those that showed signal increase, were manually defined (single polygon) and used to calculate peak ΔF/F, 50 % rise time (time from wash-in until 50 % max ΔF/F was reached), halfwidth duration and 50 % decay time (time from wash-out until 50 % decay) using ClampFit 11.1. The same regions responding to ischemia were also used to analyze synchronous activity in these slices (Figures 1H, 1M, S8, S9F, and S9G), however, using selected sub-stacks, which were normalized to F_0 images from these sub-stacks (see image analysis and plume identification). For frequency determinations, stack lengths were adapted to have at least 10 events or having a maximal length of 300 s. High Ca^{2+} event frequencies (pre- and post-ischemic 'high', Figures 1H and S9D) were analyzed in 30 s time windows around maximal activity.

To obtain ΔF/F maps of synchronous activity (Figures 2B, S4B, and S10A) maps, average intensity projections (AIPs) were obtained from peak ΔF/F frames of all synchronous events within 500 frames. Here, normalization had been performed with F average intensity projections from the beginning of the recording (F_0, 200 frames). For comparing ΔF/F maps of ischemia and glutamate application

(Figure S4B), 200 frames during the fluorescence peak were averaged and normalized with the same F_0 image. Ratio maps (Figure S4C) were calculated after binning to 32 x 32 pixels by dividing the ΔF/F map of glutamate accumulation during ischemia with the ΔF/F map of synchronous activity or exogenous glutamate application, respectively. Then, all pixel values were measured and imported to Origin Pro 2021. The three parameters were plotted pairwise with red line indicating a correlation coefficient of 1 (Figure S4D).

To quantify the signal loss of synchronous activity before the glutamate rise (Figures S8A–S8C), all events in the 150 s preceding the loss of synchronous activity were analyzed. The ΔF/F values of these events were normalized using the average ΔF/F of synchronous activity that was determined in each slice at the beginning of the recording. The resulting normalized $\Delta F/F_{norm}$ values fluctuated but eventually declined. For better comparison, the events were binned relative to the first event after which events permanently showed a $\Delta F/F_{norm}$ <0.5. Two 50 s bins were created before this event and two 25 s bins after this event, before spontaneous activity was lost in all slices.

In control slices, in which synchronous glutamate and Ca^{2+} activity and plumes were imaged over 50 min with no pharmacological applications (Figure S9), all events were analyzed in 25-300 s time windows at the beginning of the recording and after 5, 10, 20, 30 and 40 min as described above (also shown in Figures 4, 5, and 6D–6F and corresponding Supplementary Figures).

Figure 2 and related supplementary figures

Maximum intensity projections (MIP) showing plumes (Figures 2A and S10A) were calculated from 500 frames as described in image analysis and plume identification. Synchronous activity maps were generated as average intensity projections of peak ΔF/F frames of all synchronous events within 500 frames (see above). All plumes and synchronous activity occurring in these 500 frames were plotted as time traces (Figures 2B and S10A). For plume detection see image analysis and plume identification. Frequencies of plumes and synchronous activity were determined for all slices subjected to chemical ischemia at the beginning of the recording as described above. We analyzed plume half-width (HW) duration, plume intensity ΔF/F, and the ΔF/F ratio of plume intensity compared to synchronous activity in the same region of interest (Figures 2E–2H). Dashed lines reflect the plume detection limits based on intensity (ΔF/F $\geq$ 2%) and HW duration ($\geq$ 50 ms). For comparing plume parameters, only plumes for which all parameters could be characterized were considered (n = 296 plumes, Figures 2F, 2G, 3B, and 3C).

To analyze the temporal correlation between plumes and synchronous activity, the time delay between each plume and the next closest synchronous event (before or after the plume) was determined. For 189 plumes (67.7%; in total 279 plumes in 10 slices) the closest synchronous event occurred within ±5 s. For these plumes the mean time difference to the next synchronous event was 0.0034 ± 2.0836 s (mean ± s.d.). This already indicates that plumes were as likely to occur before as after a synchronous event, which is also reflected in the corresponding histogram (Figure S10D). Further, if plumes and synchronous events are fully independent, the occurrence of synchronous events in relation to a plume (i.e. an arbitrary time point zero, t_0) should follow a Poisson distribution, i.e. p (synchronous event in t±dt) = p (no event at t-dt) - p (no event at t+dt). Since the shortest time delay in either direction (pre or post plume) was determined, the effective time interval to t_0 has to be doubled and the resulting probability divided by two for positive and negative time delays (mirror function). Indeed, non-linear least-square fitting of a Poisson-like distribution using ProFit 7 (Quantumsoft) to the histogram data shows a very good agreement, since the fit gives an underlying event frequency of 0.18 Hz, which is close to the observed mean for synchronous event frequencies (0.19 ± 0.11 Hz, mean ± s.d., n = 11 slices; Figure 1H). A minor underrepresentation in the first interval can be explained by missing plumes very close to synchronous activity (based on the fitted parameters e.g. 8 additional plumes would be expected to occur within the first 200 ms). Pearson and Spearman correlations were analyzed and plotted with Origin Pro 2021 (Figures S10E and S13A).

Figure 3 and related supplementary figure

To show spatial and temporal characteristics of selected plumes, 8 single frames from the binned ΔF/F stacks were selected (Figures 3D–3G). The corresponding time course and the spatial profile are shown for the depicted circled region (full-width plume) and box, respectively. The spatial profiles are depicted after another 2x2 binning. Figure S13B shows unbinned ΔF/F data and binned raw intensity (F) data.

Figures 4 and 5 and related supplementary figures

For pharmacological characterizations, the analysis of synchronous glutamate activity, Ca^{2+} activity, and identification and analysis of plumes was performed 1 min before applying blocker and at the indicated times after application by extracting the corresponding stacks. Frequencies were determined as described above. For low event frequencies the analyzed time windows were extended from 500 frames to 6000 frames. For high plume frequencies during TBOA application they were shortened to 100 frames.

Figure 6 and related supplementary figures

For plume analysis at the indicated time point of chemical ischemia experiments (beginning of the recording, 1 min before wash-in, at 50 % signal rise, maximum signal, 1 min before 50 % decay and 4 and 10 min after 50% decay) 500-2000 frames were extracted. The standard plume analysis (Figures 6D–6F) was based on 100-1000 frames.

To visualize glutamate accumulation without plumes and synchronous activity (Figures 6C, S21A, and S21B, Middle and Bottom rows), 100 frame ΔF/F minimum intensity projections (normalized with F_0 from the beginning of the recording) were calculated and displayed with the ImageJ LUTs "Fire" and "HiLo". To display glutamate accumulation and plumes, 500 frame ΔF/F maximum intensity projections were used (Figures S21A and S1B, Top rows). For Figures 6G–6H, 200 frame ΔF/F maximum intensity projections (normalized with F_0 from the beginning of the recording) were generated to show plumes before inducing chemical ischemia (pre ischemia) and to display the spread of glutamate accumulation from defective regions during the rise phase.

Figure 7. Plume frequencies were determined as described in image analysis and plume identification at the beginning of the recording, 1 min before applying iGluR inhibitors, at the beginning of ischemia wash-in, 10 and 20 min after ischemia with inhibitors and 1 min before wash-in, at 50 % signal rise, max signal, 1 min before 50 % decay and 4 and 10 min after 50% decay of the inhibitor-free ischemia.

Supplementary movies

To create Videos S1 and S2 and 6-8, data were first reduced in ImageJ. In each stack (16-bit raw fluorescence intensity movies, 32-bit ΔF/F movies), 5 consecutive frames were averaged with the "Grouped Z Project" tool. For further reduction, the movies were converted to 8-bit with the lowest and highest values in the stacks as limits. For Videos S3, S4, and S5 no averaging was performed. The speed was adapted as indicated in the **Supplementary Movie Legends** during export at 10-100 fps to AVI files with JPEG image compression. Compressed movies were imported into VideoStudio X10 (Corel) and scalebars and application markers were added. The final movies were exported in MPEG-4 format.

Statistics

All data were statistically tested for normality (including frequencies) or log normality (for durations, rise and decay times) with the Kolmogorov-Smirnov test ($p < 0.05$) using Origin Pro 2021. As several datasets were not normally distributed, all experimental groups were compared with the Kruskal-Wallis test followed by posthoc Dunn's test (not significant ns, $^{*}p < 0.05$; $^{**}p < 0.01$; $^{***}p < 0.001$). Furthermore, duration, rise and decay times and plume sizes were tested individually against a control group with the Mann-Whitney *U* test (not significant ns, $^{*}p < 0.05$; $^{**}p < 0.01$; $^{***}p < 0.001$). Plume frequencies of individual time windows in Figure 5I were compared to control using pairwise two-sample *t*-tests (not significant ns, $^{*}p < 0.05$, $^{**}p < 0.01$). Representative ΔF/F images are displayed with the ImageJ look-up table 'fire' and the indicated scaling. Figures were assembled in Corel Draw 2018.

ADDITIONAL RESOURCES

The simulation code can be found at https://gitlab.utwente.nl/m7686441/focalglutamate_modelsimulations.